A 1-mW Vibration Energy Harvesting System for Moth Flight-Control Applications

by

Samuel C. Chang

Submitted to the Department of Electrical Engineering and Computer Science
in partial fulfillment of the requirements for the degree of

Master of Science in Electrical Engineering and Computer Science

at the

MASSACHUSETTS INSTITUTE OF TECHNOLOGY

February 2010

Author .....
Department of Electrical Engineering and Computer Science
December 28, 2009

Certified by .....
Jeffrey H. Lang
Professor of Electrical Engineering and Computer Science
Thesis Supervisor

Accepted by .....
Terry P. Orlando
Chairman, Department Committee on Graduate Students

A 1-mW Vibration Energy Harvesting System for Moth Flight-Control Applications

by

Samuel C. Chang

Submitted to the Department of Electrical Engineering and Computer Science
on December 28, 2009, in partial fulfillment of the
requirements for the degree of
Master of Science in Electrical Engineering and Computer Science

Abstract

This thesis focuses on the approach and methodologies required to build a 1-mW energy-harvesting system for moth flight control applications. The crepuscular hawk moth *Manduca sexta* is the chosen test subject. This project is part of the Hybrid Insect MEMS (HI-MEMS) program. The objective of the program is to establish an interface between adult insect neural systems, wireless communication and MEMS systems so that insects may be directed to fly to specific locations in real time.

As in all micro-air vehicles, power is one of the major concerns. A power source on the moth is required to support the flight control and wireless communication systems. There are two methods by which these payloads might be powered. The first method is to draw power from a battery, while the second method is to harvest energy from the environment. Batteries have the advantage of simplicity, while energy harvesting systems have much longer life and lower mass per total energy delivered. In addition, the total mass of circuitry, MEMS devices, and batteries may severely limit flight duration. Therefore, we have chosen the energy-harvesting method.

The energy harvesting system includes a vibration energy harvester and a boost converter that delivers power at the required 1-V level for the entire flight control system. The latest harvester has a mass of 1.28 g and output power of 1.7 mW into a matched resistive load when the moth vibrates with a ± 0.37-mm amplitude at 25.8 Hz, resulting in a ± 7.82-mm harvester amplitude.

A 2-stage AC-DC boost converter with off chip inductors has been designed and fabricated in 0.18 um CMOS technology. SPICE simulation and experiments using equivalent discrete components prove that the converter can achieve 71.68% efficiency. The test experiment of the chip will be conducted later this winter and is not included in the scope of this thesis.

Thesis Supervisor: Jeffrey H. Lang
Title: Professor of Electrical Engineering and Computer Science

Acknowledgments

This thesis was supported by the Air Force Research Laboratory as part of the DARPA HI-MEMS Program under Contract FA8650-07-C-7704. National Semiconductor Corporation provided the free chip fabrication discussed in Chapter 3. I was personally supported by a Presidential Graduate Fellowship provided by MIT. In addition, I would like to thank the Daniel Lab at the University Washington for charactarizing the body vibration of the moth and testing numorous resonators and harvesters for us. The Voldman lab at MIT and Alice Stone from the University of Arizona also helped us connect the harvester to the moth. Without their knowledge of the moth and generously providing their flight test facilities, this work would be impossible.

The iterations and construction of the harvester occured with plenty of guidance and support from Dave Otten, Frank Yaul, Francis O'Sullivan and Alejandro Dominguez-Garcia. I especially want to thank Dave for laying out the Flexible PCB, building the harvesters and implementing the discrete power electronics. I'd also want to thank Frank Yaul, the best UROP ever, for designing the ABS plastic springs such that the harvester really became flyable. Without Dave and Frank, our harvester would still be in the stone age and would have never been able to achieve the milestones.

I also want to extend a warm thank you to Professor Anantha Chandrakasan, Professor David Perreault and Professor Alex Slocum. Thank you all for spending time in giving me valuable insight into the lower power circuit, power electronics and mechanical harvester design.

I owe a huge intellectual debt to numerous individuals working at the Laboratory for Electronic and Electromagnetic Systems for their help during the development of this thesis. I would especially like to thank David Giuliano for generously helping me out with the Cadence simulations and inductor designs. Thanks Giuliano! Wei Li, Jiankang Wang, Jackie Hu, Anthony Sagneri, Yehui Han, George Hwang, Uzoma Orgi, Kevin Brokish, Robert Pilawa, Riccardo Signorelli and Warit Wichakool helped

me ease the transition into LEES early on and provided unwavering support whenever I ran into difficulties. Above all, making LEES a fun place to work.

Without my buddies at MIT, life would be completely different. Thank you Albert for being like a brother to me and giving me honest advices which really helped me become a better person. Thank you Wilt and Heechul for both being awesome roommates, great listeners and supporting me when I needed you guys the most. I would also like to thank Patrick Lin from BU fellowship for being my mentor and opening your home to me. Thank you Patrick! Last, I would like to thank Jingjing for being there for me and being ultra-supportive throughout the writing of this thesis. Thank you dear.

My parents, Peter and Carol Chang, provided much guidance and moral support during my educational career and allowed me to reach where I am today. Their care and understanding go way beyond the norm, and I am forever grateful. Your prayers gave me strength and helped me overcome all the challenges at school and in life. This thesis belongs to them as much as it does to me.

Professor Jeffrey Lang deserves my deepest gratitude. Throughout this research, he provided countless suggestions for overcoming difficult theoretical and experimental barriers. Without these critical insights, this thesis would not exist. I will never forget all the time he spent with me both during and after research meetings, even when he already had many other businesses to attend to. Furthermore, he never hesitated to remind me to rest when I had exams in the courses I was taking. Thank you so much for being patient when progresses were slow and above all, for being a great role model for me in research and in life. I cannot possibly repay all your kindness and care. Thank you Professor Lang.

Last, I would like to thank God for everything. If it was not the miracle that gave me birth and the protection and guidance throughout my life, I would not have any of these things in my life. Thank you Lord.

Contents

List of Figures

List of Tables

Chapter 1

Introduction

1.1 Background

The research conducted within the scope of this thesis is part of the Hybrid Insect MEMS (HI-MEMS) program supported by the Defense Advanced Research Projects Agency (DARPA)[1]. The objective of the program is to develop and demonstrate self-contained mobile on-insect electronics through which the motion of the insect can be controlled remotely. Thus, the electronics receive motion commands wirelessly and issue motion commands to the insect via electronic connections made to its nervous system. The on-insect electronics require a power source and it is the objective of this thesis to develop and demonstrate that power source.

DARPA and other research institutes have been interested in micro-vehicle related research since the early 1990's. One example of their interest is the Nano Air Vehicle (NAV) program[2], the goal of which was to miniaturize man-made flying vehicles to a sub-10-cm size. While such vehicles would undoubtedly have impact, severe power constraints drastically limit their mission time (~20 min), while the nature of the vehicles makes them unsuitable for unobtrusive indoor missions. The most efficient small flying machines are arguably the flying insects, which can fly for days-to-weeks at a time. In the late 1990's, the DARPA Defense Sciences Office (DSO) sought to

[1] www.darpa.mil/MTO/Programs/himems/index.html
[2] www.darpa.mil/dso/thrusts/materials/multfunmat/nav/index.htm

take advantage of insects through the Controlled Biological Systems program, the goal of which was to use insects and other small animals to collect information, for example by training them to seek out useful targets or tapping into their sensory nervous systems to monitor sensory information.

Given developments in insect neurobiology and the evolution of Microelectromechanical systems (MEMS), a new interdisciplinary approach has surfaced for achieving the desired mission capability. MEMS, which are small, light and low-power, and have a diverse set of electrical and mechanical capabilities, are the ideal man-made systems for instrumenting an insect. Insects on the other hand, have biological advantages including energy storage, efficient flight control and highly adapted sensing compared to artificial micro-vehicles. The Hybrid Insect MEMS (HI-MEMS) program, sponsored by DARPA, takes the advantage of both worlds and focuses on creating a robust long-term flight-control nano air vehicle. The crepuscular hawk moth *Manduca Sexta* was chosen to be the test platform by our team, which consists of researchers from MIT, the University of Washington and the University of Arizona.

As with all untethered micro-vehicles, on-board power is a major challenge. Solutions include long lifetime batteries, renewable energy sources, energy harvesting, etc. The goal of this thesis is to meet the energy challenge through the development of a vibration energy harvesting system capable of providing 1 mW of electrical power to the entire flight control system.

1.2 Harvester System Outline

As shown in Figure 1-1, the energy harvesting system consists of four major components: the moth body vibration, the vibration energy harvester (resonant generator), the AC-DC boost converter and the flight control battery. The moth body vibrates at a frequency of 25 Hz and amplitude of $\pm$ 1 mm in response to wing flapping. Its body vibration provides the energy scavenging source for our system. The second component is a vibration energy harvester that is a linear AC poly-phase permanent-magnet synchronous generator. This generator is supported by a resonant spring

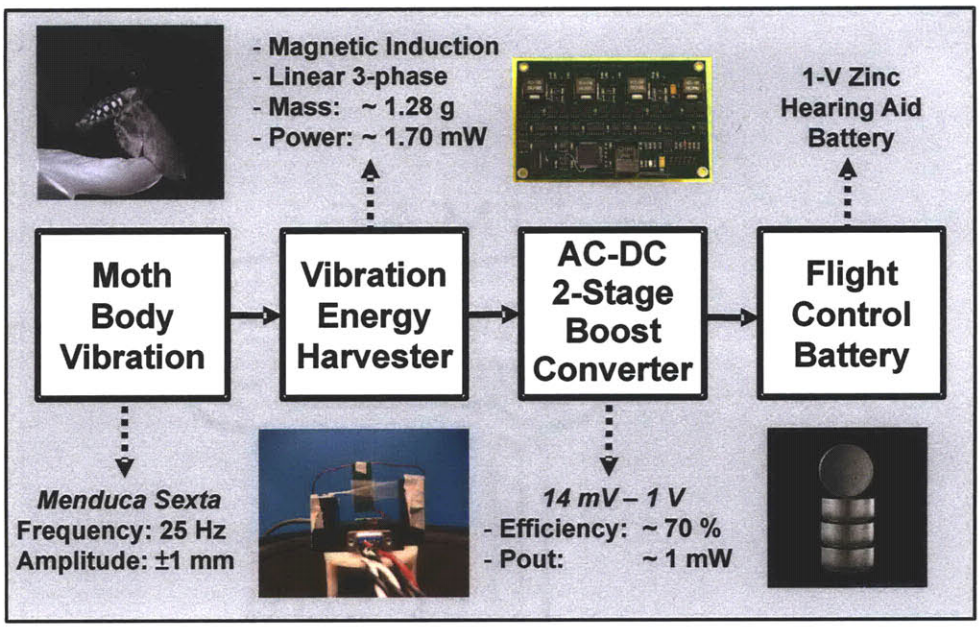

Figure 1-1: System Overview

mass structure that enhances the moth wing-flapping vibrations; the generator magnets and cores serve as the resonating mass. The third component is an AC/DC boost converter. It comprises power electronics that rectify and boost the output from the generator to charge a 1-V battery. Finally, the battery stores the harvested energy and acts as a energy source for the flight control, radio devices and the power electronics. Since the moth vibration is constrained by its own physical limitations, and the battery will be implemented by using commercially available components, the focus of this thesis is on the resonant generator and the boost converter. Design details and challenges of the two stages are given in the following subsections. At the end of this section, an overview of the results of this thesis is also given.

1.2.1 Resonant Geneator

The resonant generator comprises a support structure, moving magnets and core, and stationary windings. These parts are shown in Figure 1-2. The first three components form a spring-mass resonator tuned to the wing-flapping frequency of the moth; the structure is the spring, and the magnets and core provide the dominant proof mass.

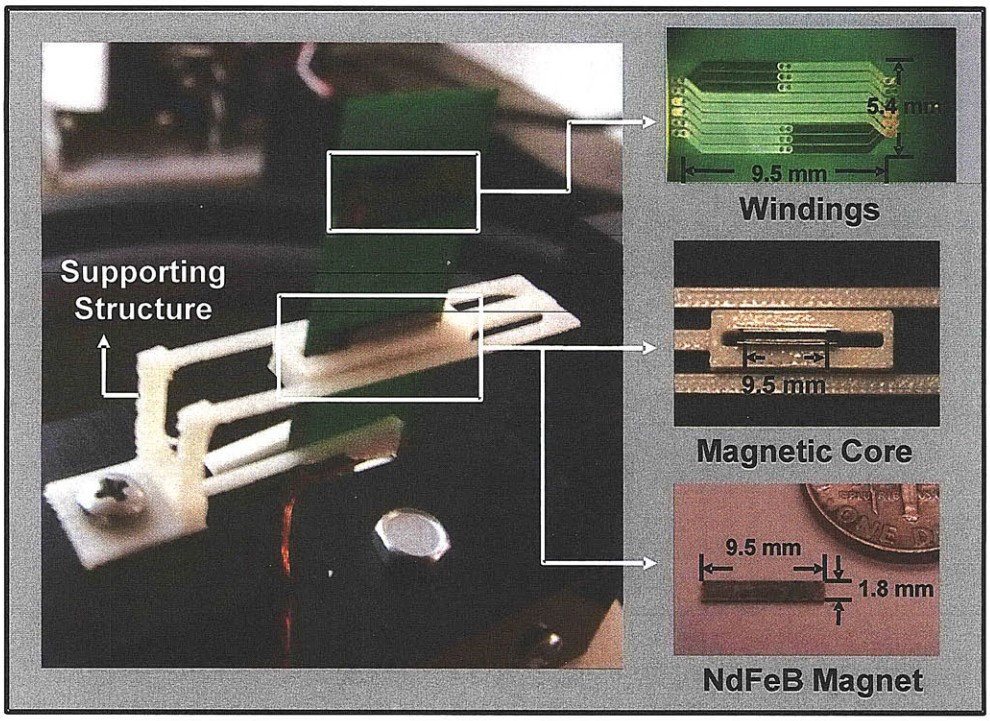

Figure 1-2: Resonant generator parts. The supporting structure made from ABS plastic was designed and fabricated by Frank Yaul.

The magnets, core and windings form the linear 3-phase AC generator.

When the moth is flying, the thorax vibration of the moth will excite the resonator which supports permanent magnets. The permanent magnets are aligned with the windings such that as the resonator vibrates, the flux through the windings varies, inducing a voltage across the windings in accordance to Faraday's law. The energy introduced mechanically into the resonator by the vibration can be extracted electronically through the electromagnetic generator.

There are several major challenges to building a resonant generator on a flying insect. The first is the harvester mass and volume limitations due to the moth's physical constraints. A typical *Menduca Sexta* has a payload capacity around 0.6 - 1.0 g, and a dorsal tent-shaped payload volume approximately 8 mm wide and 15 mm tall beneath the wings at their apex. The second challenge is the low frequency (25 Hz), low amplitude (± 1 mm) and narrow bandwidth vibration characteristic. Finally, more than 1 mW of power must be generated such that the flight control

and radio devices have sufficient operating power. In conclusion, the power density of this resonant generator must be higher than 1.67 W/kg at 25 Hz.

1.2.2 AC/DC Boost Converter

As shown in Figure 1-1, the AC-DC boost converter operates to extract maximum power from the generator, and deliver that power to a 1-VDC battery, through two stages. The first stage is a combined AC/DC rectifier and DC/DC boost converter. There is one such stage for each generator phase, and the outputs of these parallel stages deliver energy to a common intermediate energy storage capacitor at about 50 mV. Following the capacitor is a single DC/DC boost converter that raises the voltage from 50 mV to 1 V.

The two major challenges for designing the power electronics are the output characteristics of the resonant generator and the mass and volume limitations of the moth. Each winding of the resonant generator has an AC output voltage with a RMS level of 14 mV and output resistance of 0.1 Ω. This means that the power electronics must provide a high voltage conversion ratio and an extremely low input resistance. On the other hand, the physical limitations of the moth, as mentioned in Section 1.2.1, limits the use of certain topologies which use heavy inductors. This thesis will provide insight into the design, optimization, and experimentation of a high efficiency AC/DC boost converter for moth flight control applications.

1.2.3 Experimental Results

The resonant generator is capable of generating 1.7 mW of power at 25 Hz into a resistive load. The generator has a mass of 1.28 g and has been tested on a shaker table that simulates the vibration frequency and amplitude of the moth body vibration. Experimental details and a matching between the experimental results and the design model developed here is given in Section 2.4.1.

With 1.4 mW of input power from the resonant generator, the AC/DC boost converter is capable of delivering 1.059 mW of power into the load with 71.68%

efficiency. This converter was implemented with discrete components to demonstrate the validity of the topology. An integrated version of the circuit with power MOSFETs and rectification functions has been fabricated in 0.18 μm CMOS technology and waiting to be tested. Its efficiency is expected to be near 80%. Wiring losses and switching losses can be further eliminated in the integrated circuit and hence giving us a good chance of delivering more power at a higher efficiency.

With the target power delivered, the immediate future work would be reducing the system mass to below 1 g. This seems promising by means of trimming down our current structure or changing to a new structural material such as carbon fiber.

1.3 Previous Research

A careful literature survey of recent developments in the field of energy harvesting is appropriate for placing the current thesis in context. However, due to the wide range of techniques used for energy harvesting, such as exploiting chemical and thermal gradients, this thesis will limit the survey to vibration energy harvesting and insect energy harvesting.

1.3.1 Vibration Energy Harvesting

Vibration energy harvesting involves the creation of some physical structure that can couple in kinetic energy from small vibrations and convert it into storable electric energy. Due to the growing demand of autonomous sensors that must function without the need for human intervention, interest in this topic has burgeoned in recent years. Applications on the market today include shaker flashlights, ocean wave energy harvesting buoys[3], wireless sensor node energy harvesters[4], etc. Despite all these different applications for vibration energy harvesting, three main strategies of conversion dominate: piezoelectric, capacitive-based electric, and permanent-magnet-based magnetic.

[3]www.technologyreview.com/Energy/19295/?a=f
[4]www.perpetuum.com

Review papers by Roundy [1] and Mitcheson [2] have compared these three topologies and shown that although current harvester designs are still operating well below their maximum power, there has been a significant improvement with time. One of the index to evaluate the performance of a harvester is the normalized power $P_n = P/P_{MAX}$ [2]. It measures how close the performance of a specific device comes to the optimum level. Both frequency and the mass of the proof-mass are normalized in the calculation. From the data in [2] and the latest harvesters reported at PowerMEMS 2009, all harvesters have a P_n smaller than 0.2 while the harvester reported in this thesis has a $P_n = 0.36$ at 25 Hz.

Numerous research groups have focused on piezoelectric energy harvesting [3, 4, 5] due to its potential of achieving the highest converted power per unit volume. Piezoelectric materials, such as quartz and barium titanate, contain permanently polarized structures that produce an electric field when the materials deform as a result of an imposed mechanical strain. Kymissis *et al* employed unimorph strip made from piezoceramic composite material and a stave made from a multilayer laminate of PVDF foil inside sport sneakers to harvest the parasitic kinetic energy generated during walking [3]. An input signal of 1 Hz, similar in frequency to a person walking briskly, produced 20 mW peak power for the PVDF and 80 mW for the unimorph; this translates to roughly 1-2 mJ per step.

Electric energy harvesting couples vibration energy into the system by having it perform work on charges via the electric field between parallel plate capacitors [6]. In a typical scenario, charges are injected onto capacitor plates when they are closest together, meaning that the capacitance is at its maximum. Because charges of opposite polarity reside on the separate plates, the plates are attached to each other. Therefore, as vibration energy separates the two plates, it performs positive work on the charges, which are then drained from the plates when the capacitor voltage is highest, and harvested using power electronics. Besides the variable capacitor, one can also employ a layer of embedded charge, or electret, in the dielectric to carry out electric energy harvesting [7]. Such a distribution of permanent charges induces a voltage on the capacitor plates, polarizing them. As external vibration moves the

capacitor plates and alters the capacitance, charge transport along the plates delivers power to the load.

Finally, magnetic energy harvesting seeks to convert vibrational kinetic energy into an induced voltage across coils of wire, which then can deliver power to an appropriate load. This is typically done by attaching either a permanent magnet, such as that made from Neodymium Iron Boron, or a coil of wire onto a cantilever beam that is vibrationally actuated [8, 9]; the other one remains fixed. In either scenario, the coil will cut through magnetic flux as the cantilever beam vibrates, creating an induced voltage in accordance with Faraday's law.

As discussed further in Section 2.2, the magnetic vibration energy harvesting approach was chosen for our application due to the low frequency and narrow bandwidth vibration characteristics of the moth shown in Figure 2-2. On the one hand, the 25 Hz vibration frequency of the moth is too low for both variable capacitors and piezoelectrics. On the other hand, the narrow bandwidth vibration argues for a resonant harvester employing a spring and proof mass to enhance the vibration stroke, which is perfect for the magnetic harvesting approach. Detailed reasonings of the harvesting method decision are given in Section 2.2.

1.3.2 Insect Energy Harvesting

Possible alternative energy sources on the insect include thermal gradient, light, or chemical energy stored within the moth. Previous work on insect energy harvesting has compared these harvesting concepts for moths [10], studied piezoelectric-based vibration harvesters for moths [11], and demonstrated 10 $\mu W/cm^2$ thermoelectric harvesting from beetles [12]. However, to this date, none of the vibration energy harvesting methods have reported experimental data and the thermoelectric harvester generates 0.8 μW, more than 1000 times smaller than our latest output power of 1 mW.

1.4 Chapter Summary

This chapter served both as an introduction to the world of energy harvesting as well as motivation for the rest of this thesis. As noted, numerous techniques exist for harvesting energy from the environment that otherwise would have been lost. Potential energy sources include solar power, thermal and chemical gradients, acoustic noise, and vibration. Vibration energy harvesting be further divided into piezoelectric, magnetic, and electric, determined by how vibration energy is coupled into the system.

This thesis presents a road map for creating a magnetic vibration energy harvester for mass-limited 1-mW applications. The road map is divided into different sections, including electromechanical analysis, harvester design and power electronics design. For each section, an analysis shows the elements of importance in the design of a complete harvester. These analyses are connected to each other, providing a complete road map for the design of energy harvesters. Furthermore, the analyses show technology challenges where more research can improve the performance of the harvesters.

Chapter 2 gives an in-depth discussion of the simulation, optimization and experimentations of the vibration energy harvester. Through three generations of iterations, our latest harvester built with ABS plastic weighs 1.28 g and generates 1.7 mW of power into a resistive load. Additional survey of possible ambient energy sources in the system environment, and different vibration energy harvesting methods are also discussed. Chapter 3 outlines the design, simulation and experimentation of the power electronics which performs the harvester to battery voltage conversion. Finally, Chapter 4 summarizes the thesis and its conclusions, and presents possible direction of future work in this area of research.

Chapter 2

Vibration Energy Harvester

This Chapter presents the design, fabrication, and testing of a harvester that transduces the mechanical wing-flapping vibration energy from the moth into electrical energy. The target moth, *Manduca Sexta*, has a payload capacity near 1 g, and a tent-shaped dorsal payload volume approximately 8 mm wide and 15 mm tall. In addition, it's body vibrates at 25 Hz with an amplitude of ± 1 mm. Operating within these constraints, the energy harvester is designed to deliver 1 mW of electrical power at 1 VDC such that the flight control and radio system can operate properly. Based on the vibration characteristics, a magnetic induction harvesting strategy driven by permanent magnets moving past windings is chosen. A thorough electromagnetic and mechanical analysis of the harvester is developed here to provide a accurate model for optimization of the harvester. Finally, a table of harvester designs that can generate 1-mW of power and satisfy all the design constraints is generated. This table includes specific dimensions, configuration, output power and mass of the harvester design. At the end of this chapter, an optimal design is chosen, fabricated and tested.

2.1 Constraints

The design constraints of our vibration energy harvester come from the physical limitations of the *Menduca Sexta*. In this section, we first investigate the load carrying capability of the moth. This ultimately determines the upper-bound of the volume

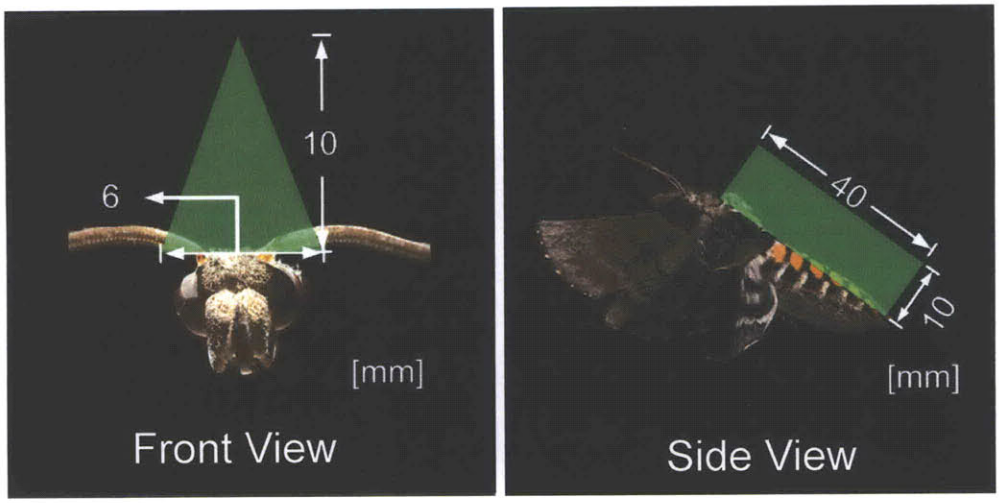

(a) Front view of volume design constraint. (b) Side view of volume design constraint.

Figure 2-1: Moth dorsal thorax design space constraint

and mass of our harvester. In addition, we need the vibration source characteristics to determine a suitable harvesting method. A thorough analysis on the moth vibration frequency, amplitude and bandwidth is given in the second part of this section.

2.1.1 Payload Mass and Volume Constraint

The payload capacity of *Manduca Sexta* on its dorsal thorax is around 0.6 - 1.0 g. The mass of the harvester should be less to accomodate additional payloads, some to be powered by the harvester. The dorsal payload volume is tent shaped and is shown in Figure 2-1. It has a 6-8 mm base, and a 10-15 mm height beneath the wings when they close at the apex of their flapping motion. The length of this volume can be 4-5 cm so long as the harvester mass distribution does not affect the flight balance of the moth.

2.1.2 Moth Vibration Characterization

The characterization of the vibration source is essential in deciding which harvesting method to implement and in determining the output power limits. For our vibration harvesting system, the source is the thorax movement of *Menduca Sexta* during flight.

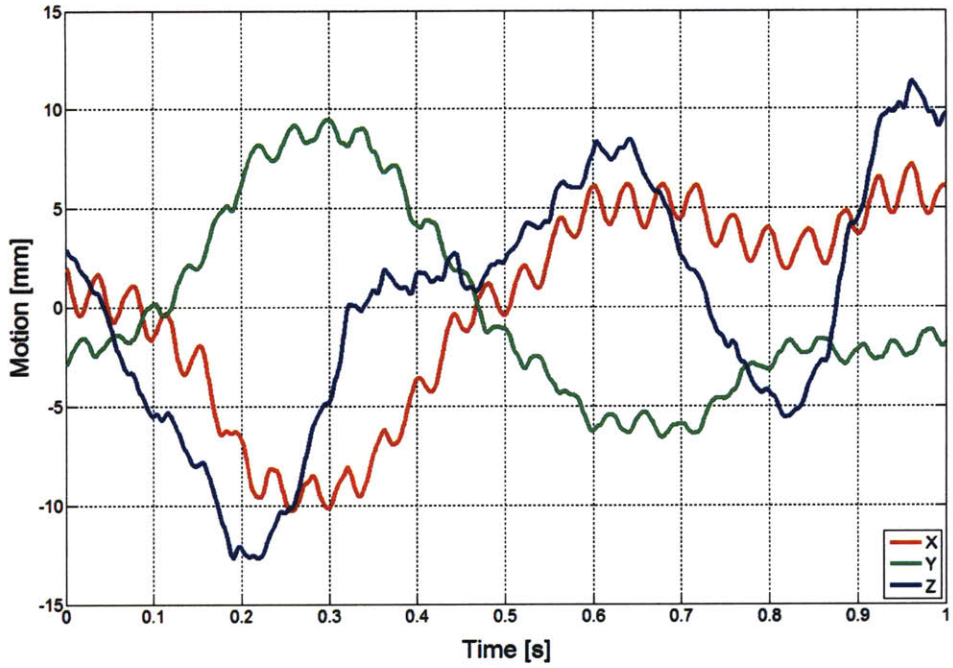

(a) Three dimensional moth movement tracked by high speed video camera. Raw data provided by the Daniel Lab at UW.

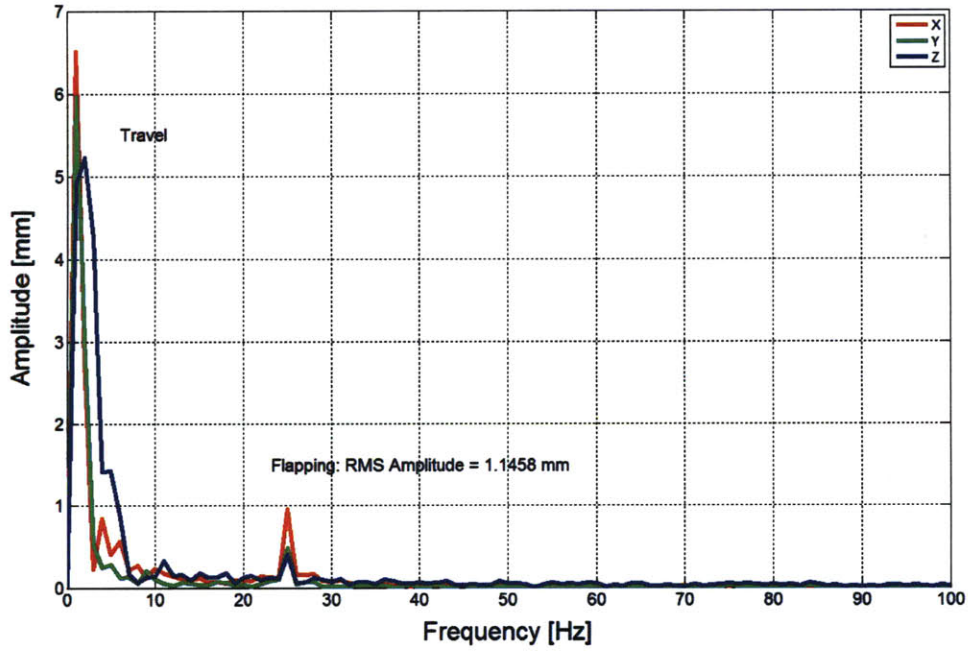

(b) Fourier Transform of moth motion shows that the moth thorax vibrates at 25 Hz with an amplitude of 1.1458 mm.

Figure 2-2: Moth flight motion characterization

Using high-speed video cameras, colleagues from the Daniel Lab at UW tracked the three-dimensional inertial motion of a moth during flight. A graph of the three dimensional movement is shown in Figure 2-2(a).

The vibration characteristic in which we are interested is its amplitude and frequency. This is seen in the Fourier transform of the three dimensional inertial movement of the moth. As shown in Figure 2-2(b), the moth thorax vibration has an amplitude of 1.1258 mm and frequency of 25 Hz normal to the dorsal side of the thorax. It can also be seen from Figure 2-2(b) that the vibration frequency has a relatively narrow bandwidth. These vibration characteristics were observed from one moth, but additional experiments indicate that there is little variation from moth to moth. According to these vibration characteristics and physical limitations of the moth, we will explore various harvesting strategies in the following section and determine one that would acheive our goals.

2.2 Harvesting Strategy

MEMS vibration energy harvesters have employed a number of different approaches to transduce mechanical energy into electrical energy for end use. These methods include variable capacitors, piezoelectric, variable inductors, permanent electric and permanent magnet. These strategies have their own merits for vibration sources of different frequency, amplitude and physical design space limitations. As shown in Figure 2-2, our vibration source is the low frequency, low amplitude and narrow bandwidth thorax wing-beat vibration of the insect while flying. In addition, the payload has volume and mass limitations of approximately 2.4 cm^3 and 0.6 g.

First, let us consider variable capacitors. In order to generate 1 mW of power at 25 Hz, the harvester has to generate 40 μJ/cycle. Taking into account the energy stored in the capacitor ($\frac{1}{2}\varepsilon_0 E^2$) and the electric field limit of 10^6 V/m, the capacitor would have to store 4.4 J/m^3. By dividing the required energy per cycle by the maximum energy density density, the minimum required air-gap volume for the variable capacitor harvester is determined to be approximately 9.1 cm^3, nearly 4 times larger than

the payload volume limit of the moth. Therefore, the variable capacitor harvesting method is not feasible.

Next, let's investigate the piezoelectric harvesting approach. The kinetic force on the piezoelectric material can be expressed as $MA\omega^2$, where M is the mass of the proof mass, A is the vibration amplitude of the piezoelectric material and ω is the vibration angular frequency. Considering the payload mass and volume shape limit, we can assume the proof mass to be 0.1 g with a vibration amplitude of 5 mm. The vibration angular frequency is determined by the moth's vibration frequency of 25 Hz. The maximum kinetic force on the piezoelectric material is therefore 12 mN and the output voltage can be calculated using the following equation:

$$V_{out} = g_{33} \times F \times T/S \tag{2.1}$$

where g_{33} is the piezoelectric constant, F is the kinetic force, T is the thickness of the material and S is the cross sectional area of the material. If we substitute the piezoelectric constant of 0.02 Vm/N and assume the material thickness to be 0.1 mm and cross sectional area to be 3 mm^2, we can obtain the output voltage. The output voltage is 3 mV which is too small for power electronics to convert to 1 V. Therefore, the piezoelectric method cannot be implemented here due to the low frequency of the wing beat which results in a low output voltage.

Finally, let us consider variable inductors and permanent electrets. The variable inductor method generally requires too much stationary mass, hence decreasing the allowable proof mass. A lower proof mass would then greatly limit the output power. In addition, it is more complex and lossy than systems with permanent magnets, particularly at small size scales. As for permanent electrets, they have a very low energy density and poor stability in comparison to permanent magnets.

The only remaining approach is the permanent magnet topology. Additionally, the narrow bandwidth of the moth vibrations, as shown in Figure 2-2, argues for a resonant harvester employing a spring and proof mass to enhance the vibration stroke. A stroke of about $\pm$ 8 mm is allowed beneath the wings at the top of their motion.

To achieve a 1-mW power output then requires the conversion of 40 mJ during each cycle with a peak force of 2.5 mN, assuming 100% energy-conversion efficiency from the generator and its attendant power electronics. This is again incompatible with small low-mass, low voltage capacitive or piezoelectric energy conversion, and so a magnetic-based harvester is selected here.

2.3 Resonant Generator

2.3.1 Overview

The resonant generator comprises a plastic spring, moving magnets, an iron core, and stationary windings. The first three components form a spring-mass resonator which is tuned to the wing-flapping frequency of the moth of 25 Hz. In the spring-mass resonator, the magnets and core provide the dominant proof mass. The magnets, core and windings form the linear poly-phase AC generator.

One of the earliest concerns of our approach was whether or not the moth would fly with a resonator on its dorsal thorax. Figure 2-3(a), shows a snap-shot of the moth carrying a resonator during flight. It clearly demonstrates that a moth can and will fly while carrying a resonant energy harvester. This is an important proof that our approach to designing the energy harvester is possible and reasonable. Figure 2-3(b) is one frame from a movie which shows our latest ABS plastic resonator attached to the moth. The movie demonstrates that wing flapping is unaffected by the resonator, even when the resonator is elevated on a pedestal. The blurred motion of the moving mass is visible at the top of the photograph.

In the following parts of this section, we will give an overview of the mechanics of each component in the resonant generator in order to aid the understanding of the vibration energy harvester.

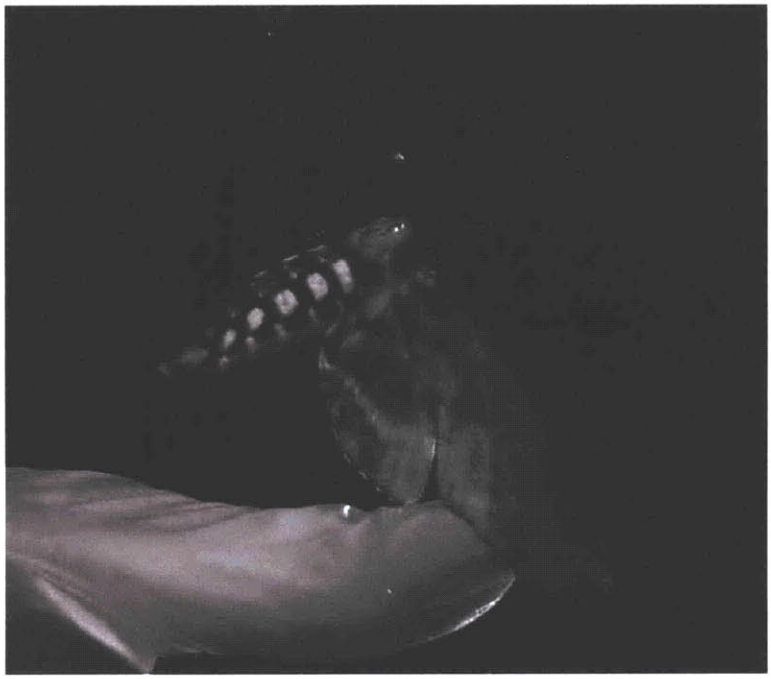

(a) Moth taking off of the researchers thumb while flying with a resonating spring attached to its dorsal thorax. This resonator was implemented by Dr. Alejandro Dominguez-Garcia, a post-doc in the Lang Lab at MIT.

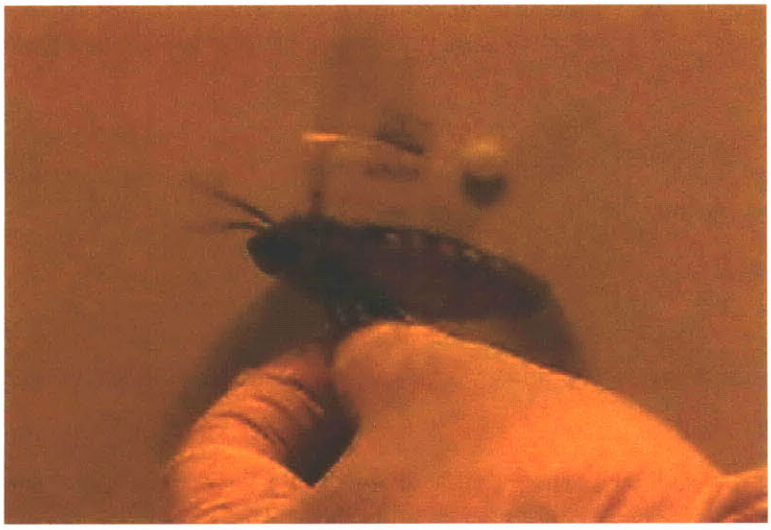

(b) Moth flapping its wings with plastic resonant generator attached to its dorsal thorax. This moth took off with the resonator afterwards and was never recovered. The experiment was conducted by Wei Mong Tsang from the Voldman Lab at MIT.

Figure 2-3: Snapshots of the moth flying and flapping its wings with the resonator attached to its dorsal thorax. This demonstrates that the moth can and will fly with the resonator.

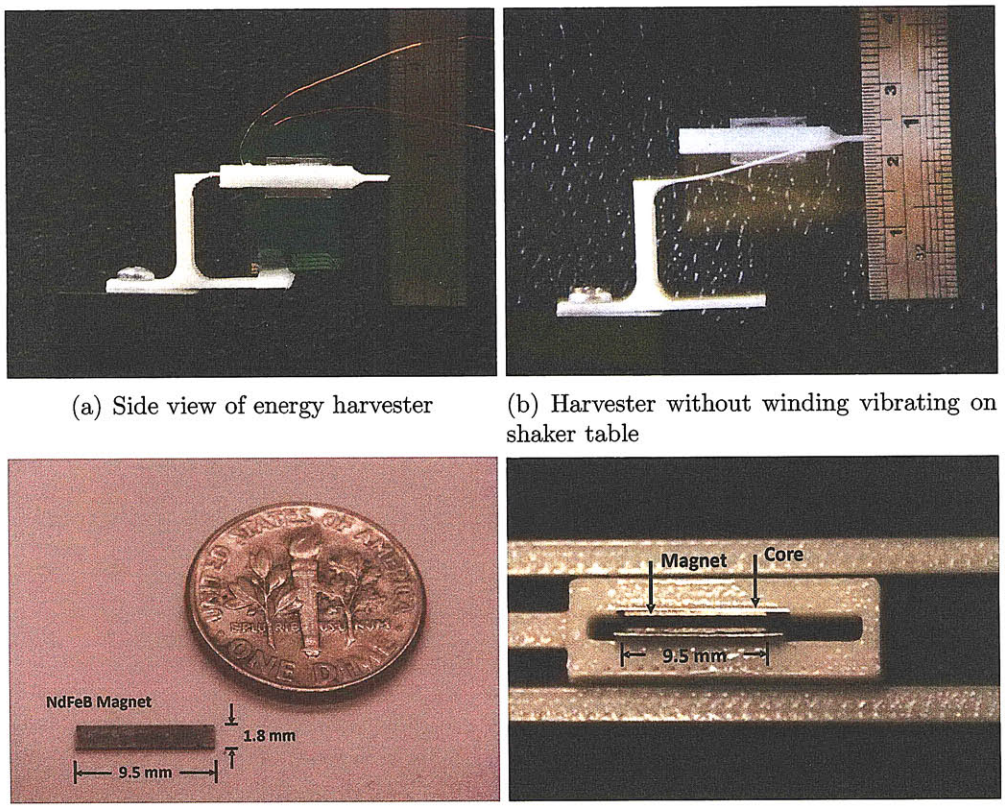

(a) Side view of energy harvester

(b) Harvester without winding vibrating on shaker table

(c) NdFeB magnet size compared with the dime.

(d) Top view of the NdFeB magnet and magnetic core inside the ABS plastic spring.

Figure 2-4: ABS plastic harvester fully assembled with the magnetic core and flexible printed circuit board. The ABS components were designed and fabricated by Frank Yaul, an undergraduate in the Lang Lab at MIT.

Spring

The spring is folded to be compact, and carry the magnets and cores level as they sweep vertically past the printed-circuit windings. The setup of the spring with the magnetic core aligned with the flexible printed-circuit winding is shown in Figure 2-4(a). The blurred motion in Figure 2-4(b) shows the spring vibrating on a shaker table which simulates the vibration motion of the moth. To limit horizontal motion, the spring is split into a left-half and right-half spring. In Figure 2-4(b), only one half spring can be seen; the second spring is behind the first. Both halves of the spring can be seen more clearly from Figure 2-4(d).

The spring and its holding structure are printed in 3D from acrylonitrile butadiene

styrene (ABS) plastic. The ABS plastic material is measured to have a 0.9-1.1 g/cm^3 mass density, a 2.1-GPa elasticity modulus, and a safe 0.6% yield strain. The ABS is printed layer-by-layer in orthogonal plys with a 0.07-in minimum feature size. The ABS components were designed and fabricated to the specification derived here by Frank Yaul, an undergraduate in the Lang Lab at MIT.

Magnets and Magnetic Core

The magnets and magnetic cores, held by their ABS carrier, are shown in Figure 2-4(d). Spring segments from both sides can be seen at the top and bottom of the photograph while the air gap between the coil and the core is 100 μm on both sides. Three NdFeB magnets, each 9.5 mm wide, 1.8 mm tall, and 0.3 mm thick, are stacked vertically along 0.2-mm-thick cores attached to the carrier on each side of the air gap; there are six magnets in total. These magnets each have a magnetization of 1.5 Tesla and were manufactured by Magnetic Component Engineering Inc[1]. A single magnet is shown in Figure 2-4(c). The magnets are magnetized across their thickness to drive magnetic flux across the air gap. Their magnetization reverses from magnet to magnet along the cores in the direction of travel to form a three-pole magnetic structure.

Multi-pole Windings

Figure 2-5(a) illustrates what one phase of the energy harvester's winding arrangement would look like when manufactured using a two-layer flexible printed circuit implementation provided by Altaflex. The windings are double sided, with sets of conductors on one side of a separating layer connecting with sets of conductors on the other side to form the individual coils. Typically a multiphase arrangement of windings would be used to maximize the amount of energy converted by the energy harvester. The winding pattern over a single magnet pole for a six phase winding arrangement is shown in Figure 2-5(b).

[1] www.mceproducts.com

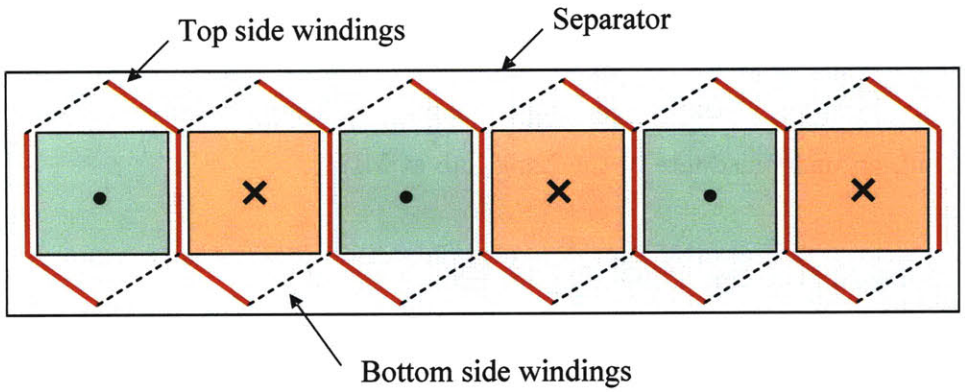

(a) Illustration of one phase of the energy harvester winding arrangement which comprises of six coils. The solid conductors are on the top, and the dashed conductors are on the bottom. Connections between the two layers are made with plated-through vias shown as black dots in the figure.

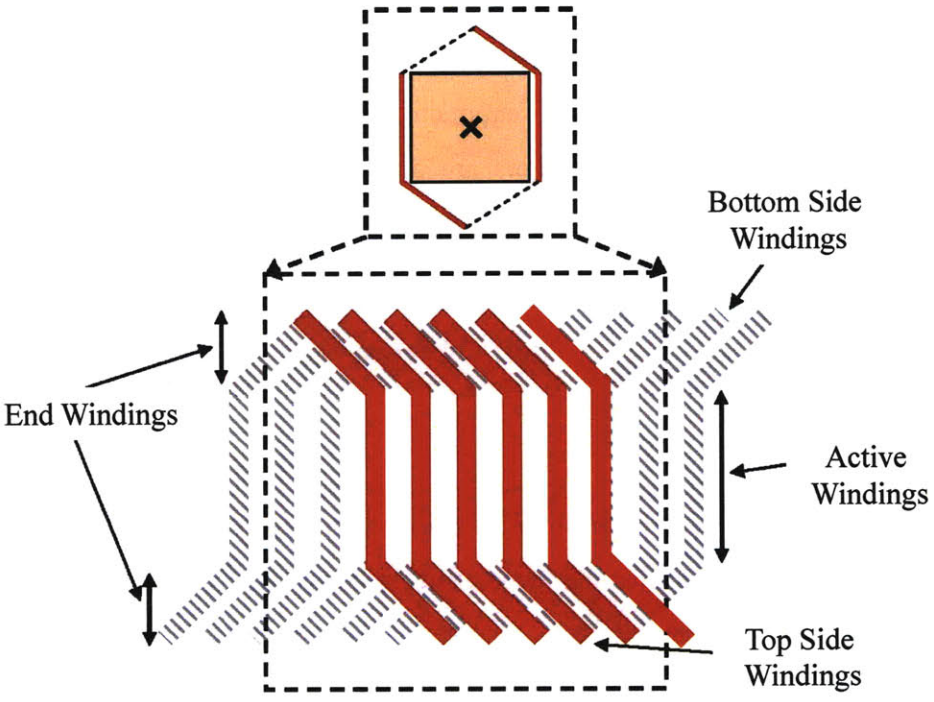

(b) Winding pattern over a single pole for a six phase winding arrangement manufactured using the Altaflex winding process.

Figure 2-5: Configuration of the multi-pole flexible printed circuit board.

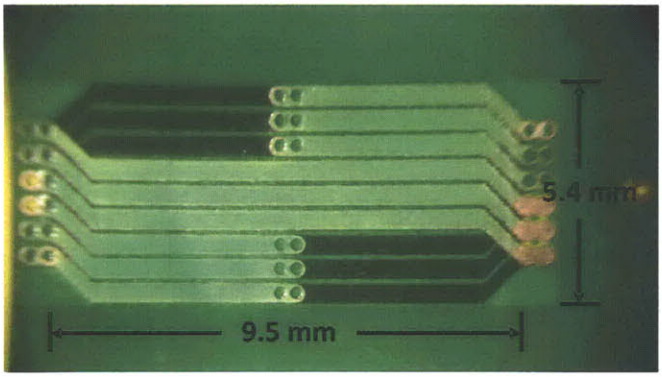

Figure 2-6: Flexible printed circuit board under microscope. The winding layout was drawn by David Otten, a research scientist in the Lang Lab, and manufactured by Altaflex.

Design Rule	High Density	Standard
Minimum Trace / Space (Subtractive Etch)	0.001"/0.0015" (0.33 oz.)	0.0015"/0.002" (0.33 oz.)
Minimum Via Hole Diameter (Before Plating)	0.0015" (UV Laser)	0.003" (UV Laser)
Minimum Blind Via Diameter (Before Plating)	0.004" (UV Laser)	0.008" (UV Laser)
Trace to Edge Distance	0.001" (UV Laser)	0.003" (UV Laser)
Trace to Edge Tolerance	0.0005" (UV Laser)	0.001" (UV Laser)
Cover Layer Aperture Positional Tolerance	0.001" (Laser Defined)	0.003" (Cover Film)

Table 2.1: Altaflex flexible printed circuit board process capabilities and tolerances.

Figure 2-5(b) illustrates that the winding pattern for a multiphase winding arrangement can be very complicated. Some important features of the winding process include the need for end windings. These are necessary in order to allow the coils to complete, but they add to parasitic loss in the windings. Other winding design dimensions include wire thickness, wire width, multi-phase and multi-layer configurations. As with all designs, there are also design constraints due to the process capabilities. Table 2.1 shows an abstract of the process capabilities and tolerances provided by Altaflex[2]. For our harvester coil design, the most critical one is the trace to insulator space ratio. This process constraint limits the maximum coil density and the lowest possible parasitic resistance and effectively limits the output power of the harvester. These design flexibilities and process constraints were fully explored in our work and incorporated into our optimization program written in MATLAB. The code can be found in Appendix A.

[2]www.altaflex.com/capabilities.htm

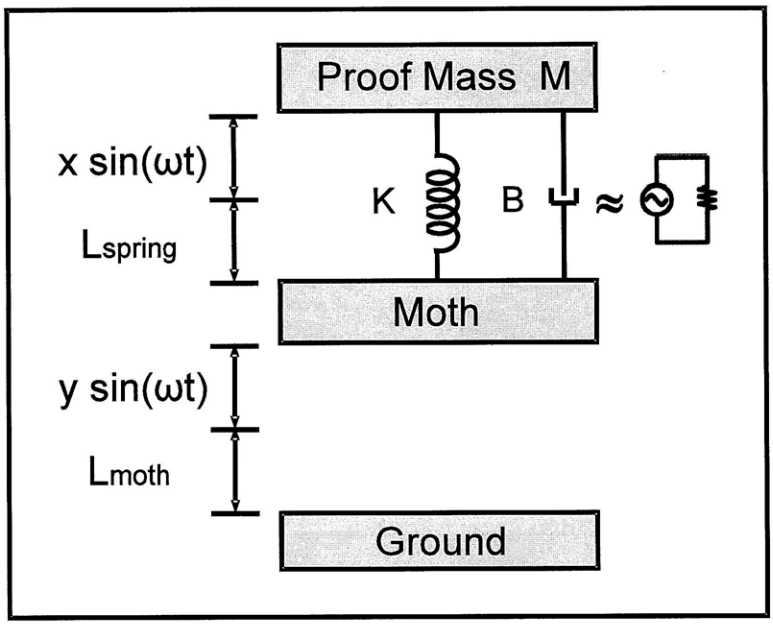

Figure 2-7: The resonant converter modeled as a spring-mass-damper system.

The three-phase windings as fabricated by Altaflex are shown in Figure 2-6. They are fabricated from two-sided 37-mm-thick printed-circuit copper on 13-mm-thick Kapton. Each phase winding contains two coils in a figure-eight pattern that can link flux from two magnets. The windings match the 9.5-mm length of the magnets, and their vertical pitch matches the 1.8-mm magnet width as shown in Figure 2-4(c). The winding terminations are located to permit easy stacking of a multi-layer winding. The generator in Figure 2-4(a) has two stacked layers.

2.3.2 Spring-mass-damper Model

The mechanical model of our resonant converter is shown in Figure 2-7. The body vibration of the insect can be modeled as a sinusoidal vibration source with an amplitude of y relative to the inertial ground and angular frequency of ω. On top of the insect, lays a resonator with proof mass M and spring constant K. L_{spring} is the unstressed length of the spring, and L_{moth} is the average height of the moth during flight.

The proof mass vibration can also be modeled as sinusoidal with an amplitude

x relative to the moth's body and frequency of ω, same as the moth vibration frequency. The electromagnetic coupling, which converts kinetic energy to electrical energy, along with energy loss in the harvesting system is represented as a viscous damper of damping coefficient B (newton-seconds per meter). The total force on the proof mass F_{tot} consists of the spring force F_s and the damping force F_d. We can then express the total mechanical force F_{tot} as

$$F_{tot} = F_s + F_d \tag{2.2}$$

The spring force F_s can be expressed as

$$F_s = -kx \tag{2.3}$$

The damping force may be mathematically modeled as a force synchronous with the velocity of the object but opposite in direction to it. If such force is also proportional to the velocity, as for our simple mechanical viscous damper (dashpot) model in Figure 2-7, the force F_d may be related to the velocity u by

$$F_d = -Bu = -B\dot{x} \tag{2.4}$$

Finally, treating the proof mass as a free body and applying Newton's second law, the total force F_{tot} is

$$F_{tot} = ma = m\left(x + y + L_{moth} + L_{spring}\right)'' = m\left(x + y\right)'' \tag{2.5}$$

where m is the mass of the proof mass, and a is the acceleration of the proof mass relative to the inertial ground.

With the relationships given in Equation (2.3), (2.4) and (2.5), we can rewrite Equation (2.2) as

$$F_{tot} = F_s + F_d \tag{2.6}$$

$$-m \cdot \ddot{y} = m \cdot \ddot{x} + B \cdot \dot{x} + k \cdot x \tag{2.7}$$

Solving the differential equation (2.7) in sinusoidal state, we get

$$m\omega^2 \cdot Y = -m\omega^2 \cdot X + j\omega B \cdot X + k \cdot X \tag{2.8}$$

where X and Y are the complex sinusoidal amplitudes of x and y, respectively. At resonance, the first and third term on the right hand side of Equation (2.8) cancel. Since we are interested in the amplitude of the resonator vibration, we obtain

$$X = \frac{m\omega Y}{B} \tag{2.9}$$

The mechanical power going into the damper is

$$P = \frac{1}{2} B\omega^2 X^2 \tag{2.10}$$

We can combine Equation (2.9) and (2.10) and obtain the following relationship

$$P = \frac{1}{2} B\omega^2 \left(\frac{m^2\omega^2 Y^2}{B^2} \right) \tag{2.11}$$

$$= \frac{m^2 Y^2 \omega^4}{2B} \tag{2.12}$$

From Equation (2.12), we can see that the only design variable remaining is the damping factor B. Y and ω are respectively the vibration amplitude and frequency of the moth which are given constants. On the other hand, the mass of the resonant converter m is limited by the moth's mass carrying constraints given in Section 2.1. Therefore, in order to harvest more mechanical energy through the damper, a lower damping factor is more desirable. However, from Equation (2.9), this results in a large amplitude X. There is therefore a maximum harvester power output given a

maximum X and a maximum m. If we combine Equations (2.9) and (2.12), we can get the following relationship

$$P = \frac{1}{2} m\omega^3 XY \tag{2.13}$$

which expressed power in terms of dimensional constraints. By applying a vibration amplitude $X = 5$ mm and proof mass $m = 0.2$ g to Equation (2.13), we can get an estimated output power of 1.936 mW.

2.3.3 Electromagnetic Analysis

In this section, we will focus on analyzing the electromagnetics of the resonant generator. The amount of power that can be extracted from the energy harvester is a function of the voltage that can be induced by the resonant generator and the resistance of the harvester's windings. For an electromagnetic energy converter the voltage generated, V, can be expressed as the time derivative of the flux linkage λ such that

$$V = \frac{d\lambda}{dt} \tag{2.14}$$

This equation can be reorganized as

$$V = \frac{d\lambda}{dy} \cdot \frac{dy}{dt} \tag{2.15}$$

where y is the relative position between the magnet and the winding as shown in Figure 2-9. The relationship in Equation (2.15) indicates that the voltage is propotional to the displacement derivative of the flux linkage and the relative velocity between the magnet and the winding. This means that it is desirable to have the energy harvester's windings passing through a strong magnetic field as fast as possible. In addition, the key to understanding the operation of the resonant converter, is to determine $\frac{d\lambda}{dy}$, or equivalently $\lambda(y)$. A number of magnetic designs were studied during the course of this work in an effort to identify the most suitable design for the cyborg

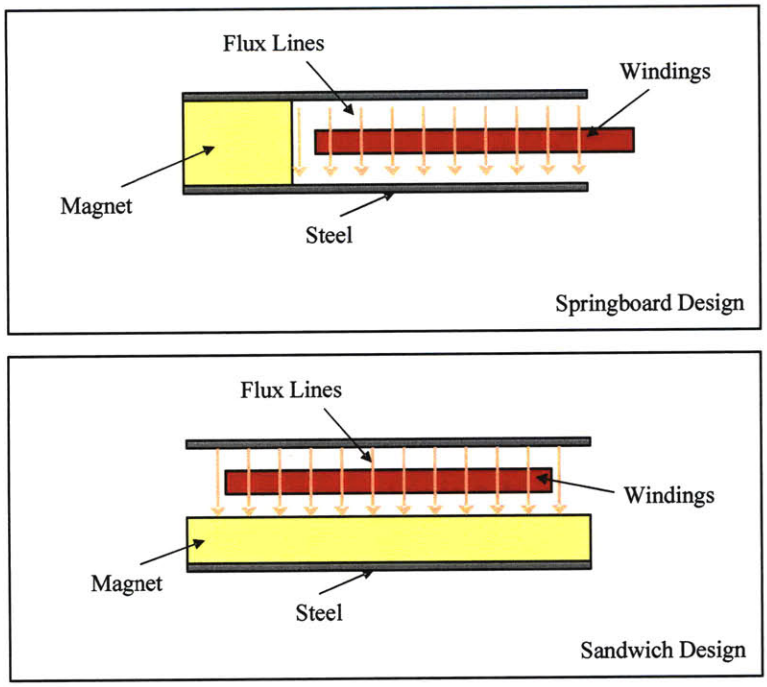

Figure 2-8: The springboard and sandwich magnetics designs that were studied as part of the design process for the energy harvester. In these two designs, the windings move into and out of the page.

moth energy harvester. The two that were examined in most depth are shown in Figure 2-8.

The first design is referred to as the springboard design, while the second design is referred to as the sandwich design. In both designs, the windings move into and out of the page. The magnets, on the other hand, are stacked into the page with alternating magnetic polarization from magnet to magnet as shown left-to-right in Figure 2-5(a). Of the two magnetics designs, it is the sandwich design that results in a magnetic field distribution that is more suitable for use within the energy harvester. The reasons for this are due mainly to the fact that the sandwich design results in a more uniform magnetic field distribution in the air-gap than is the case with the springboard design.

Evaluation of the magnetics designs was carried out using the COMSOL Multiphysics (CMP) finite element method software suite. Using CMP it was possible to analyze the magnetic field distributions in the air-gap through which the energy

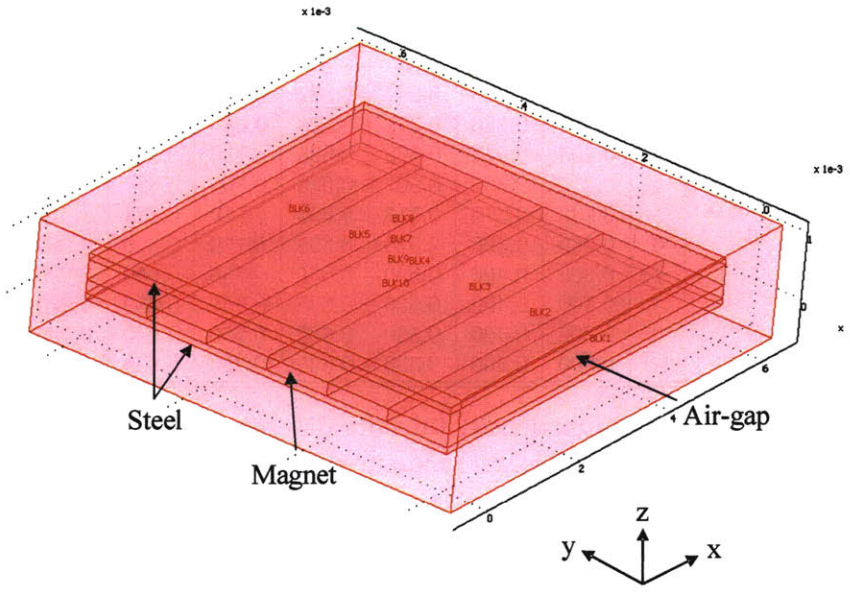

Figure 2-9: Illustration of a six pole sandwich type magnetics design in the CMP user interface. These magnets each have a magnetic flux density of 1.5 T. Their magnetic flux is in the z-direction and the magnetization reverses from magnet to magnet in the y-direction of travel to form a six-pole magnetic structure. Our final two designs were three-pole and four-pole magnetic structures.

harvester windings would pass. The power and design utility of CMP lies in the fact that the program allows the fast evaluation of how changes in the magnetics design affect the magnetic field distributions in the air-gap. Figure 2-9 illustrates what a sandwich type magnetics design looks like when drawn using the CMP user interface.

The approach which we took to evaluate the $\frac{d\lambda}{dy}$ inside the magnetic core was to take a few critical geometries of the magnetic core and use COMSOL to determine the peak magnetic flux density. This would give us a table of magnetic flux densities corresponding to core geometries as shown in Table 2.2. Then, we can use interpolation to find the magnetic flux density peaks for other geometries. This table is used in the simulation described in Section 2.3.4 as a look-up/interpolation table to determine the magnetic field strength. The magnetic flux inside the core did not saturate in the COMSOL simulations.

A very important point that must be mentioned here is that increasing the air-gap would greatly decrease the peak and average magnitudes of the magnetic flux density.

		MT / PP						
		0.2	0.3	0.4	0.5	0.6	0.7	0.8
MW / PP	0	0	0	0	0	0	0	0
	1	0.165	0.216	0.267	0.377	0.487	0.594	0.700
	2	0.188	0.280	0.371	0.526	0.680	0.840	1.000
	3	0.195	0.347	0.500	0.625	0.750	0.910	1.070
	4	0.216	0.362	0.507	0.628	0.750	0.897	1.043
	5	0.238	0.376	0.513	0.632	0.750	0.883	1.017
	6	0.260	0.390	0.520	0.635	0.750	0.870	0.999
	7	0.300	0.400	0.530	0.635	0.750	0.860	0.999
	8	0.300	0.400	0.530	0.635	0.750	0.850	0.999
	9	0.300	0.400	0.530	0.635	0.750	0.840	0.999
	10	0.300	0.400	0.530	0.635	0.750	0.830	0.999

Table 2.2: Average magnetic flux density table for different magnetic core geometries. The average magnetic flux densities were measured in the middle of the air gap where the coils will be placed. Each magnet has a magnetic strength of 1.5 T. MT, MW and PP are respectively the magnet thickness in the direction of the magnetic flux, the magnet width and the magnetic core plate-to-plate distance.

A 100 μm air-gap increase would lead to an average magnetic flux density decrase of 0.1T. Therefore, fabricating a small air-gap device would be a big challenge for the project. Nevertheless, this means that for any given energy harvester design, it is desirable to have as small an air-gap as possible. Alternatively, if a larger air-gap is required, a thicker magnetic material is needed to create sufficient magnetic flux density in the air-gap. The tradeoff is an increase in the total mass. Therefore, an optimization of the tradeoff between power and mass is required to determine the optimal solution for our design with manufacturing constraints having a significant influence.

2.3.4 Simulation

In order to find the design that can generate the most power while satisfying the moth payload mass and size limitations, and all fabrication limitations, we implemented an optimization process in MATLAB code shown in Appendix A. The optimization sweeps all possible design parameters including core and magnet dimensions, coil configurations and the resonator vibration amplitude. Design rules of the coil, shown in Table 2.1, and the resonator vibration amplitude limit, defined by the moth payload shape limit, were also taken into account.

For each design, the core and magnet dimensions were first applied to a magnet flux density look-up table, generated by magnetic simulations in COMSOL, to determine the magnetic flux density that passes through the coils. Once the magnetic flux density is determined, the simulation substitutes different coil configurations, vibration amplitudes and load resistances into the mechanical model to obtain the output voltage and power. The output voltage is derived from Equation (2.14), and the average output power is derived from this voltage, the harvester resistance and the load resistance.

An important point that must be made here is that the open circuit voltage of the harvester, is not a constant AC voltage source. This is because the load resistance will affect the vibration amplitude of the harvester. A smaller load resistance will create a larger damping effect on the harvester and as a result decrease the amplitude and velocity of the vibration. The decreased velocity will then decrease the open circuit voltage. Since the open circuit voltage is a function of the load resistance, the maximum output power does not necessarily happen at the matched load condition. We can express the output voltage across the load resistance as follow

$$V_{load} = \left[\frac{\alpha}{1+\alpha}\right] \cdot V \tag{2.16}$$

where V_{load} is the voltage across the load, α is the ratio between the load resistance and the output resistance of the harvester, and V is the open circuit voltage. The load voltages were calculated for different vibration amplitudes and load resistances of the same harvester design. Therefore for each harvester design, there exists an optimal load resistance which yields maximum output power. This phenomenon is confirmed in experiments in Section 2.4.2.

Finally, we sum up the mass of all the components and calculate the output power from the load voltage. Therefore, for each design, we would have its output power and total mass along with specific design details.

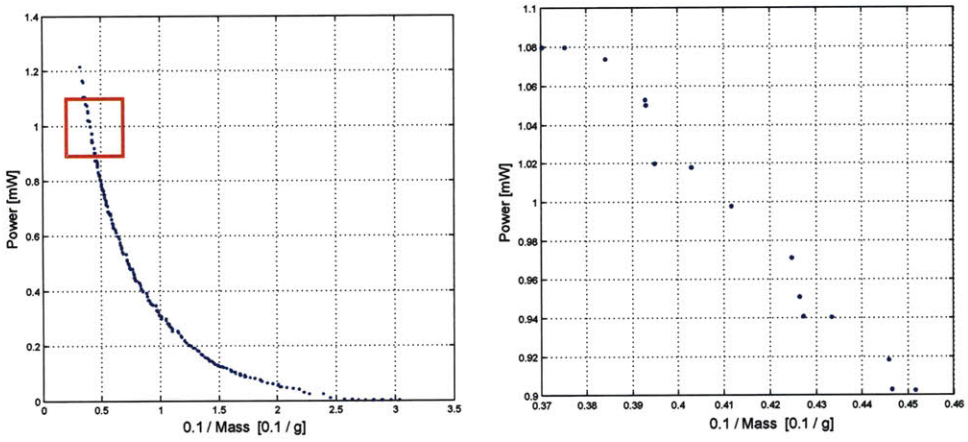

(a) Harvester output power to mass tradeoff curve.

(b) Zoomed in harvester output power to mass tradeoff curve.

Figure 2-10: Harvester optimal design curve. Designs in the red box are magnified in (b) and its detailed designs specifications are shown in Table 2.3.

Overall		**Magnet**				**Winding**			
Output Power	Mass	Quantity	Thickness	Width	Length	Phases	Cells	Layers	Width
$[mW]$	$[g]$	$\sharp$	$[mm]$	$[mm]$	$[mm]$	$\sharp$	$\sharp$	$\sharp$	$[mm]$
1.0798	0.266	4	0.3	1.5	9	3	2	2	0.4
1.0798	0.270	3	0.3	1.8	9.5	3	2	2	0.5
1.0736	0.260	3	0.32	1.7	9.5	3	2	2	0.5
1.0529	0.255	3	0.3	1.8	10	3	2	1	0.5
1.0498	0.254	3	0.32	1.6	10	3	2	2	0.4
1.0198	0.253	4	0.3	1.5	8.5	3	2	2	0.4
1.0178	0.248	3	0.32	1.7	9	3	2	2	0.5
0.9975	0.243	3	0.32	1.6	9.5	3	2	2	0.4
0.9711	0.235	3	0.32	1.7	9.5	3	2	1	0.5
0.9510	0.235	3	0.3	1.6	10	3	3	1	0.4
0.9407	0.234	3	0.3	1.9	8.5	3	2	1	0.5
0.9404	0.231	3	0.32	1.6	10	3	2	1	0.4
0.9184	0.224	3	0.32	1.7	9	3	2	1	0.5
0.9032	0.224	3	0.3	1.6	9.5	3	3	1	0.4
0.9025	0.221	3	0.34	1.5	9	3	2	2	0.4

Table 2.3: Harvester optimal design table with magnet and winding design details. The two designs at the top of the table were chosen as they generate the maximum power and satisfy the mass constraint.

2.3.5 Final Design

In order to compare the tradeoff between the output power and mass, the performance of each design generated in the optimization code was plotted on a 2-D graph with the x-axis being the inverse mass and y-axis being the output power. Designs that have higher output power and higher inverse mass are more desirable. The resulting graph identified the optimal design curve shown in Figure 2-10. Each point indicates a specific design capable of generating that much power with a total mass as shown on the figure. The x axis of the two curves is one tenth of the inverse of the total mass of the system. Though this expression may seem confusing initially, this representation gives an intuitive sense of designing a system with higher output power (positive y direction) and lower mass (positive x direction). From Figure 2-10, the tradeoff between output power and mass can easily be observed. A special note is that the lower-left corner of Figure 2-10 was originally filled with design points. However, these points have larger mass and smaller output power compared to the optimal design curve, and therefore were taken out of Figure 2-10 for clarity.

Since the flight control system requires more than 1-mW of power, we will focus on the designs in the upper-left box shown in Figure 2-10(a),which are capable of delivering 1-mW of power but also light enough for the moth to carry. Figure 2-10(b) is the zoomed in figure of the box in Figure 2-10(a), and Table 2.3 gives more details for the designs in Figure 2-10(b). Of all the designs, we selected the top two designs listed in Table 2.3 due to their high output powers and RMS voltages. Both designs were fabricated but only the second design in the table was tested since it has a higher RMS output voltage compared to the first design. In addition to the information given in Table 2.3, the second design, also known as the 3-magnet design, is expected to have a 0.098 Ω output resistance, 0.852 coil copper fraction and 0.575 T average magnetic flux density. Of the total mass of 0.27 g, the core, magnet and winding contribute 0.101 g, 0.115 g and 0.05 g respectively. The 3-magnet design was successfully fabricated, built and tested. Experimental results are given in the following section.

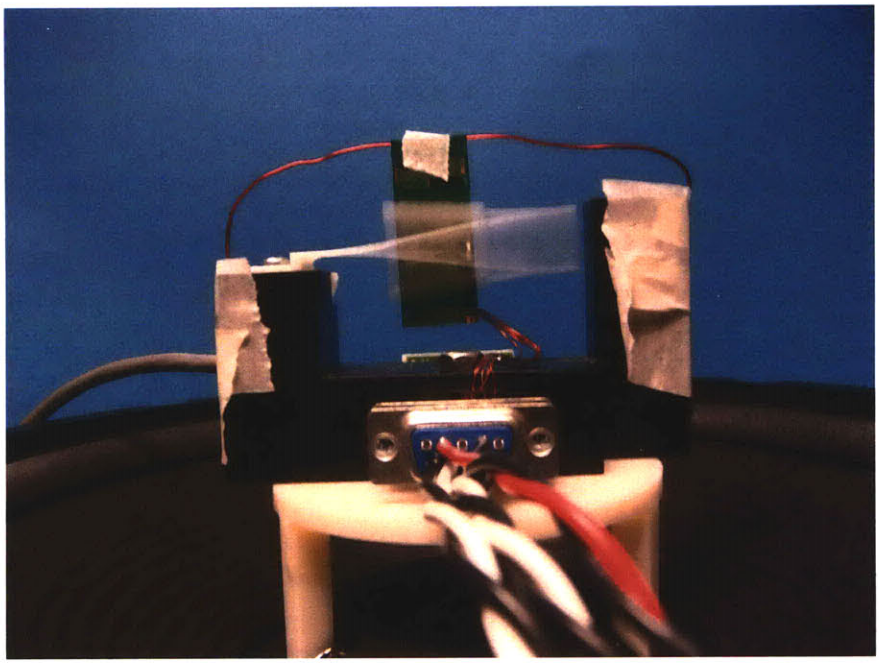

Figure 2-11: Harvester vibrating on shaker table

2.4 Experiments

A successful energy harvester not only needs to be simulated in MATLAB but also built and demonstrated. This section will attempt to bridge the gap between simulation results and an actual energy harvester. Two experiments are performed in this section. The first is the output voltage measurement of the harvester connected to a matched resistive load. The harvester is put on a shaker table which mimics the thorax vibration of the moth and the output voltage waceforms across the resistive load are compared to our simulation to verify the accuracy of our resistance and $\lambda(y)$ model. In our second experiment, we will load the harvester with a variable resistance in order to verify the optimal resistance ratio between the load and the harvester internal source resistance. A comparison between between the experimental data and our model expectation is given.

The harvesters tested in this section were all based on the second design in Table 2.3 which has a three magnet configuration. It successfully generated 1 mW of power. However, if this power is passed through the power electronics, which are discussed in

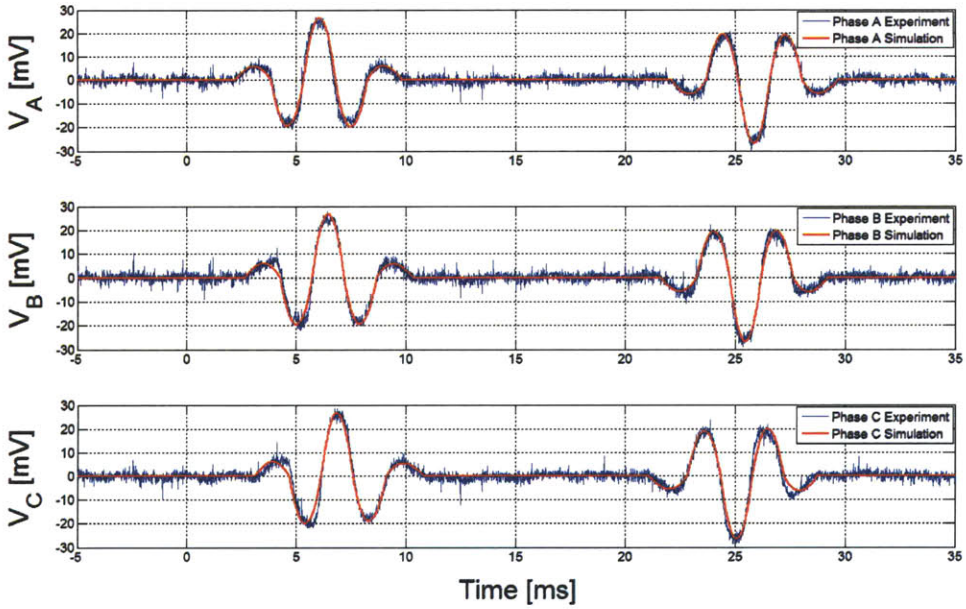

Figure 2-12: Loaded harvester 3-phase voltage waveforms compared with MATLAB simulation results

the next chapter, the final output power would be less than 1 mW. Therefore, in order to meet our intermediate goal of getting 1 mW of power out of the power electronics, we attempted to increase the output power of the harvester during the course of the experiment by means of increasing the number of magnets from three to six. Three magnets were put on both sides of the windings instead of the original design which has three magnets only on one side of the windings. The model was also refined to a six magnet configuration and compared with the experimental data. The following two subsections show the experimental results of the six magnet design.

2.4.1 Harvester Voltage Measurement

Figure 2-11 shows the generator components assembled on a shaker table. The printed-circuit windings are stabilized from above, and supported by thin winding connections from below. An accelerometer, barely visible in the rear, is attached to the shaker frame. Connections to the power electronics are at the bottom of the photograph.

Figure 2-12 shows balanced three phase 0.110-W-loaded load-voltage waveforms

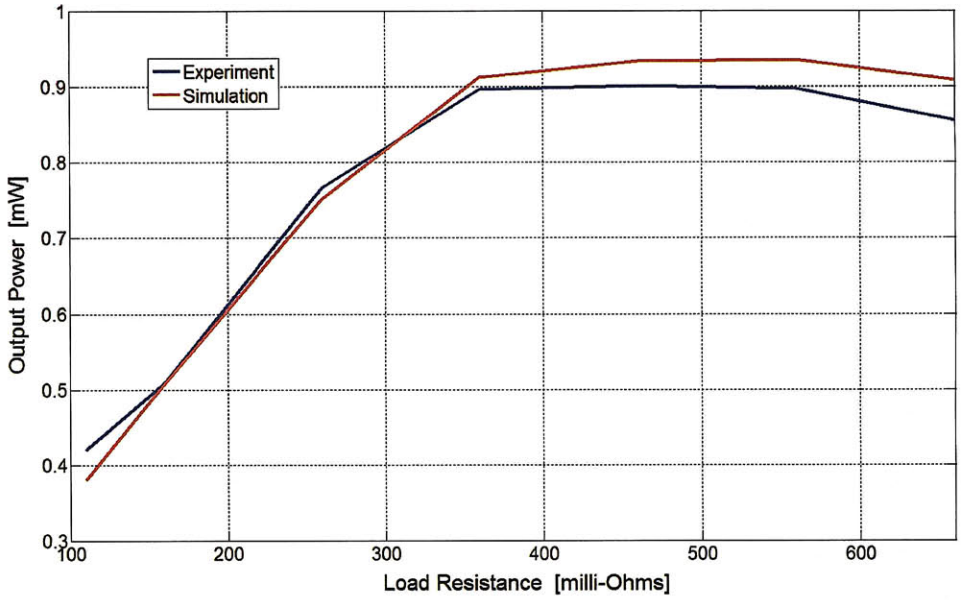

Figure 2-13: Output power versus load resistance tradeoff. Simulation and experiment are matched nicely with maximum output power happening at 450 milli-ohm load resistance.

when the shaker vibrates with a ± 0.37-mm amplitude at 25.8 Hz, resulting in a ± 7.82-mm generator amplitude, and a 1.7 mW output power to the load. By dividing the generator vibration amplitude by the shaker vibration amplitude, the Q of the loaded harvester is determined to be 21.1. The resonator Q without windings is approximately 65 and decreases to 40 when the windings without resistive load are added. Therefore, we can observe that the relative size of the mechanical losses compared to the electromagnetic coupling are small.

The harvester has an output resistance of 0.118 Ω, and the air-gap between the two metal plates of the core is 1.3 mm. The modeled generator terminal voltages are shown for comparison. From Figure 2-12 we can see that the experimental results of the harvester output voltage match nicely with the simulation results from our MATLAB code. This indicates that the resistance and $\lambda(y)$ models which we developed are accurate and good for future iterations.

2.4.2 Harvester Optimal Load Experiment

To explore the output power, the generator phases are loaded with balanced resistors of various values. The shaker is set to vibrate with a ±0.23-mm amplitude at 25.8 Hz. The resulting output power into the load resistors is shown in Figure 2-13 as a function of load resistance. The peak output power near 0.9 mW, which occurs with a generator amplitude of ±7.0 mm, does not come with a matched load of 118 mΩ due to the electromechanical loading of the generator. In this experiment, the generator amplitude varies from ±2.4 mm to ±8.4 mm as the load resistance increases. The Q of the resonator without windings is around 65 and decreases to 40 and 20 respectively when the winding and resistive loads are added. This is a good indication that the mechanical friction loss of our harvester is relatively small and the damping mostly comes from the electromagnetic coupling.

2.5 Chapter Summary

This chapter mapped out the mechanical and magnetic theoretical foundations behind the operation and design of our resonant generator. The resonant generator was tuned to resonate with the 25-Hz body vibration of the *Menduca Sexta* moth during flight and transduce the mechanical vibration energy of the moth into electrical energy via the electromagnetic coupling between permanent magnets and coils. The dimensions of the magnet and layout configuration of the coils were optimized in MATLAB such that the harvester is capable of generating 1 mW of power while having a mass less than 1 g.

Based on our optimized design, the harvester was built and tested. The latest harvester has a mass of 1.28 g and output power of 1.7 mW into a matched resistive load when the shaker vibrates with a ±0.37-mm amplitude at 25.8 Hz, resulting in a ±7.82-mm generator amplitude. The resonant converter output voltage waveforms were also compared to our simulation and the two match nicely as shown in Figure 2-12. The close match between the experimental results and the model indicates that a 1-mW vibration energy harvester operating at 25 Hz is indeed realizable and that our

harvester model is capable of accurately predicting the performance of the harvester. As for the mass, it is still too large for a moth to carry, however, by means of trimming down the ABS plastic support structure and exploring lighter and stronger materials such as carbon fiber, a 1-mW resonant generator weighing less than 1 g is possible. A third generation design achieving 0.99 mW and 0.93 g with the same input vibration but smaller harvester vibration amplitude has been produced since the writing of this thesis.

The remaining chapters of this thesis build upon the established foundations of the resonant generator. In particular, Chapter 3 investigates the power electronics, which are used to convert the energy generated by the harvester to a higher voltage level, capable of charging a 1-V battery. Different topologies will be evaluated and simulated in Cadence.

Chapter 3

Power Electronics

A 1-mW vibration energy harvester was designed and tested in the previous chapter. However, the low AC output voltage characteristic of the harvester brings the need for power electronics to rectify and convert the voltage to higher and more usable levels for the flight control system.

There are four major challenges for the power electronics. The first two challenges are due to the characteristics of the harvester. The first challenge is the low voltage level of the harvester output. The harvester output voltage is an AC voltage with a typical 14 mV RMS value. This greatly limits the use of devices which require higher voltage drops, such as diodes. The second challenge which the harvester presents is its source resistance which is around 0.1 Ω. The low output resistance of the harvester requires the use of low resistance power MOSFETs and inductors. Low on-state resistance MOSFETs are realized by making the channel width of the transistor larger. This brings a tradeoff in creating larger gate capacitances and hence limitations in the operation frequencies of the power electronics where low loss is required. Low loss is critical for a harvester since the harvester must power this loss beyond the useful load.

The third challenge comes from the physical space and load limitations of the moth. For the hawk moth, it has a design space of 0.6 cm^3 on top of its back and a maximum carrying capacity of 1 g. Therefore, anything larger or heavier than these limits, such as large inductive components with heavy magnetic cores, are

probably unsuitable for our application. The final challenge is the large conversion ratio between the energy harvester output voltage, which is 14 mV, and the flight rechargeable system battery, which requires 1 V to be charged.

The low output voltage level and small source resistance of the harvester combined with the physical limitations of the moth and the high conversion ratios needed for the power electronics are the four major factors in deciding the power electronics topology. These issues will be addressed by smart chip layout techniques and inductor designs. The topology decision process, design techniques and experimental verifications of the power electronics are given in this chapter.

3.1 System Overview

This section will describe the decision process of our power electronics design. We start by addressing the challenges stated in the opening of this chapter and find an optimal topology that could meet all the specifications in the process. Let us first consider the design constraints of the power electronics.

3.1.1 Design Constraints

The first design constraint that warrants consideration is the moth's payload mass limitation. Since the ultimate goal of this project is to have the energy harvesting system, which includes the resonant generator and the power electronics, weigh less than 0.6 - 1 g, the power electronics has to be as integrated as possible.

Next, a CMOS process capable of handling the voltage levels in our system must be chosen. The highest voltage in the power electronics is the final output voltage of 1 V. A 0.18 μm CMOS process would be a good choice since it has a normal operating voltage of 1 V with some special processes that can handle voltages up to 5 V. With respect to process performance, it is a mature and robust process that does not suffer large transistor leakage effects associated with more advanced CMOS processes. Additionally, since our circuit clock speed will be in the kilo-hertz regime, the process speed of the 0.18μ CMOS process would be more than sufficient. With the support

from National Semiconductor Corporation[1] (NSC), we obtained the SPICE model files for its 0.18 CMOS process and were able to simulate the transistor performances in Cadence and aid our circuit topology selection process.

The final constraint is the operating frequency. Understanding the upper-bound of the circuit operation frequency would aid the topology decision process as each topology has a frequency spectrum in which it performs the best. The frequency constraint of the power electronics comes from the output resistance of the harvester. From our simulation and experimental confirmation in Section 2.4.1 and 2.4.2, the harvester has an output resistance of approximately 0.1 Ω with an optimal load to source resistance ratio between 4 and 5. Therefore, in order to get the most output power, the power electronics should extract power while behaving like a 0.4 - 0.5 Ω resistance. As for each MOSFET, we hope that the on-state resistance can be in the order of 0.01 Ω. In order to achieve low on-state resistances, wider MOSFETs were required. However, this also increases the gate capacitances and hence the dynamic power losses due to charges and discharges of the gate capacitance during transistor switching.

Taking into account the tradeoff between the on-state resistance and gate capacitance, we attempted to search for the maximum operating frequency such that the dynamic power loss is less than 1 μW, 1% of the 1-mW output power. The maximum operating frequency was determined to be 200 kHz by simulations carried out in Cadence. This frequency limitation automatically eliminates converter topologies which typically require higher operating frequencies such as the resonant converters. The remaining topologies are the multi-stage boost converter and the switched capacitor boost converter.

The two remaining topologies each have their strength and weaknesses. The multi-stage boost converter's greatest strength is its high efficiencies for high conversion ratio applications. However, it requires the use of high Q inductors which can only be achieved in discrete circuit components. On the other hand, the switched capacitor boost converter can be completely integrated. The major drawback of it is the bottom

[1] www.national.com/analog

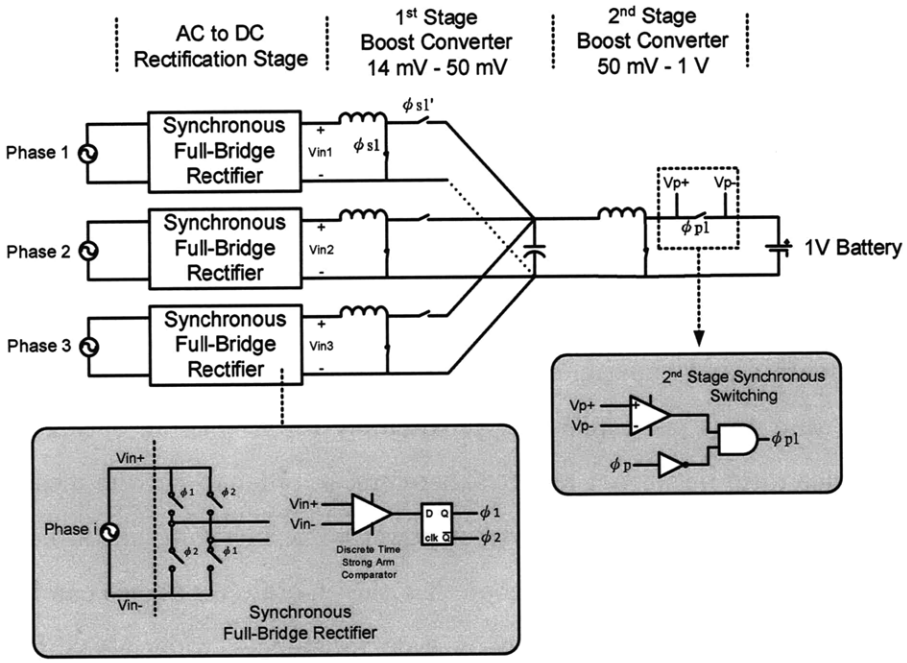

Figure 3-1: System overview of the two-stage boost converter.

plate capacitance which can be as large as 10% of the capacitor itself. This results in a 10% power loss for each charge and discharge action for each capacitor. In addition, since our conversion ratio is nearly 100 fold, the switched capacitor topology would require at least tens of capacitors even with smart switching configurations. This would result in a power loss more than the output power of the harvester. Therefore, we selected the two-stage boost converter shown in Figure 3-1.

3.1.2 Two-stage Boost Converter

As shown in Figure 3-1, the two-stage boost converter takes in the 3-phase AC output voltages from the resonant generator and then rectifies them with three seperate full-bridge rectifiers. Digital StrongARM comparators [13] are implemented in the full-bridge rectifier to reduce power loss. The rectified AC voltages are then passed through the first stage boost converter which boosts the voltage to 50 mV. The output energy is held by an intermediate low DC resistance capacitor of 10μF between the

first and second stage. Finally, the second-stage DC-DC boost converter boosts the voltage to 1V. The capacitor and the inductors used in the convereter are implemented with discrete components in order to increase the quality factor and overall efficiency. The capacitor would ultimately be integrated on-chip while the inductors probably cannot be integrated. However, in future designs, the inductors might be moved into the harvester windings. All other power electronics components will be integrated in a 0.18 μm CMOS process. Details of the design and optimization of the two-stage boost converter are given in the following section.

3.2 Two-stage Boost Converter Design

In this section, we first give an introduction to the concept of a inductor based boost converter. Next, we optimize the two-stage boost converter. An optimization code, which can be found in Appendix A.2, is implemented in MATLAB to find the optimal design parameters. In order to minimize the power MOSFET power losses and reduce the mass of the circuit, the power MOSFETs are fabricated in 0.18 μm CMOS technology. Layout issues are addressed in this section. The inductor optimization and fabrication is discussed seperately in Section 3.3.

3.2.1 Boost Converter Concept

The boost converter, which would be used in both stages of our two-stage boost converter, is shown in Figure 3-2. V_{in} and V_o are the input and output voltages, while R_H represents the output resistance of the harvester in the first stage and the DC resistance of the capacitor in the second stage. R_S, on the other hand, is the DC resistance of the inductor. The on-state resistances of switches S_1 and S_2 are not shown in Figure 3-2 but are represented as R_{S1} and R_{S2} in the following equations.

The boost converter operates in two phases, ϕ_1 and ϕ_2. During ϕ_1, switch $S1$ is on and switch $S2$ is off. The current comes out of voltage source V_{in}, goes through its output resistance, R_H, then flows through the inductor L and switch S_1, and finally comes back to V_{in}. The current and voltage relation during ϕ_1 can be expressed as:

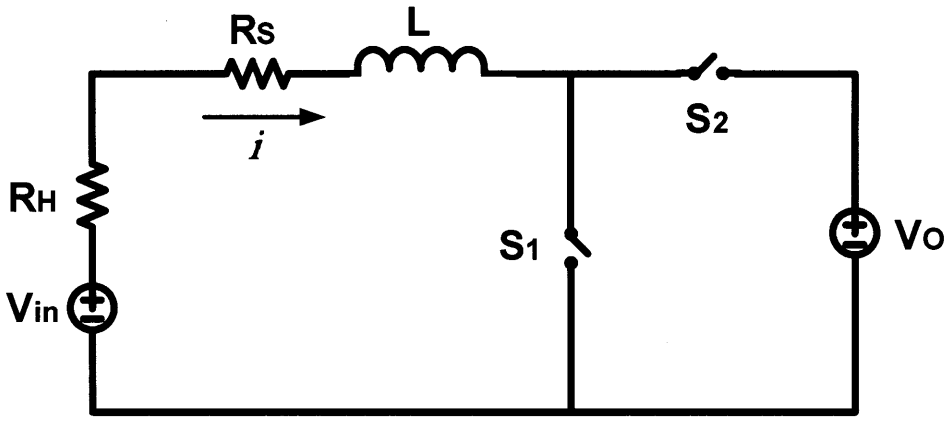

Figure 3-2: Boost converter circuit.

$$\frac{di_1}{dt} = \frac{1}{L}V_{in} - \frac{1}{L}\left(R_{S1} + R_S + R_H\right) i_1 \tag{3.1}$$

where i_1 is the current going through the inductor during ϕ_1. When the circuit goes into ϕ_2, switch $S1$ turns off and switch $S2$ turns on, creating a direct current path between the input voltage source V_{in} and the output voltage source V_O. The current and voltage relationship during ϕ_2 is then:

$$\frac{di_2}{dt} = \frac{1}{L}\left[V_{in} - V_o - \left(R_{S2} + R_s + R_H\right) i_2\right] \tag{3.2}$$

where i_2 is the inductor current during ϕ_2. If we assume the duty cycle of ϕ_1 to be D and the entire converter period to be T, we can express the relationship between i_1 and i_2 as

$$i_1(DT) = i_2(0) \tag{3.3}$$

since the inductor current at the end of ϕ_1 and at the beginning of ϕ_2 have to be the same. Equation (3.3) sets the first boundary condition. Similarly, at the end of ϕ_2, the boost converter comes back to ϕ_1.

$$i_2((1-D)T) = i_1(0) \tag{3.4}$$

With differential equations of the boost converter given in Equation (3.1) and (3.2) along with the boundary conditions given in Equation (3.3) and (3.4), we can now start the optimization process of finding the converter design which has the best efficiency.

3.2.2 Optimization

This section focuses on the design optimization of the two-stage boost converter. Parameters to be optimized include the inductor inductance, L, the operating frequency, f, and the intermediate voltage level between the two stages. The properties of the switches will be determined by the National 0.18μm CMOS process while the harvester output voltage and resistances have been previously determined in Chapter 2. Each of the above parameters will be optimized in a systematic approach. Let us first consider the power MOSFETs.

In order to save space and mass, it makes most sense to fabricate our power MOSFETs into a single chip rather than having heavy discrete components connected on a printed circuit board. With the National 0.18 μm process tech file in hand, we characterized the MOSFET's characteristics under Cadence simulations. The most important characteristic when investigating MOSFET energy efficiencies, is the tradeoff between the source-drain on-state resistance and the gate capacitance. The on-state resistance would lead to a DC power loss when the current flows through the transistor channel. The power loss due to the on-state resistance can be expressed as the following:

$$P_{DC} = i_{DS}^2 R_{on} \tag{3.5}$$

where i_{DS} is the drain to source current and R_{on} is the on-state resistance. On the other hand, the gate capacitance would be charged and discharged whenever a switch is being turned on and off. If we assume the switching frequency to be f and the gate capacitance to be C, the dynamic switching loss can be expressed as:

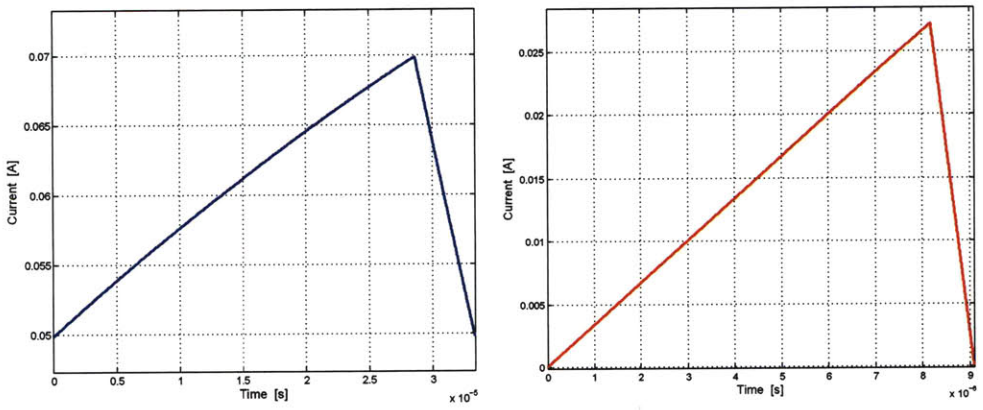

(a) First stage inductor current

(b) Second stage inductor current

Figure 3-3: Inductor currents in the first and second stage of the boost converter. Operating conditions and expected performances of the two boost converters are shown in Table 3.1.

$$P_{dyn} = CV_{DD}^2 f \tag{3.6}$$

Equation (3.5) and (3.6) may seem independent at first glance but since R_{on} and C both depend on the transistor channel width, W, they are closely correlated. If the gate resistance needs to be reduced, the easiest way is to increase W which effectively increases the cross area of the current path and hence lowering the resistance. However, by increasing the channel width, the overlap area between the gate and the transistor's source and drain is increased. This leads to an increase in the gate capacitance. Therefore, an increase in the transistor channel width would lower P_{DC} but on the other hand increase P_{dyn}. By running simulations in Cadence, we were able to find the relationship between R_{on}, C and the channel width W and implement it into the optimization code listed in Appendix A.2.

With the power MOSFET tradeoff between dynamic power loss and DC power loss investigated, we can begin the parameter sweep. These parameters include the converter switching frequency, f, duty cycle, D, inductor, L and intermediate voltage, V_o. For every set of parameters, the first stage and second stage transient current waveforms, $i(t)$ was calculated by solving Equations (3.1), (3.2), (3.3) and (3.4). The

(a) First stage boost converter design table

Eff.	Voltage		Power				Design Parameters			Switch Parameters		
η	Vo	Vin	Po	Pin	P_{dc}	P_{dyn}	f	L	D	W	R_{on}	C_{gs}
85	50	14	0.41	0.48	0.06	0.01	30	10	85	0.4	2.92	264.5
[%]	$[mV]$		$[mW]$				$[kHz]$	[μH]	[%]	[m]	[mΩ]	[pF]

(b) Second stage boost converter design table

Eff.	Voltage		Power				Design Parameters			Switch Parameters		
η	Vo	Vin	Po	Pin	P_{dc}	P_{dyn}	f	L	D	W	R_{on}	C_{gs}
98	1	0.05	1.18	1.20	0.009	0.003	100	10	95	0.4	2.92	264.5
[%]	$[V]$		$[mW]$				$[kHz]$	[μH]	[%]	[m]	[mΩ]	[pF]

Table 3.1: 2-stage boost converter design parameters.

current waveforms can be seen in Figure 3-3. We then can calculate the output power, P_{out}, the power losses which include DC power loss due to series resistance, and the dynamic power loss due to transistor switching. Our optimization was based on getting the most output power rather than the highest efficiency since the entire moth flight control system is more concerned of receiving sufficient power from the harvesting system. Finally the optimization results are shown in Table 3.1.

3.2.3 Chip Layout

The first step in chip layout is to determine how many power transistors could be put on the chip. As shown in Table 3.1, the transistors have an equivalent channel width of 0.4 m in order to lower the on-state resistance. Hence they will take up the majority space of the chip. After laying out the transistors, we found that the maximum number of transistors we could put on the chip was eight, for the given chip size of 3 mm by 3 mm. The 3 by 3 millimeter area was the maximum size permitted by NSC for the free fabrication process. Since our entire three phase converter requires 20 transistors, it would be impossible to put the entire converter onto the chip given the available process from NSC. Therefore, we decided to implement only one phase with its first and second stage boost converter on the chip. The full bridge rectifier would use four transistors and the two stage boost converters would use two each.

Even though it would be nice to have the entire system onto one chip, our one phase per chip approach provides better testability and also the flexibility to build the

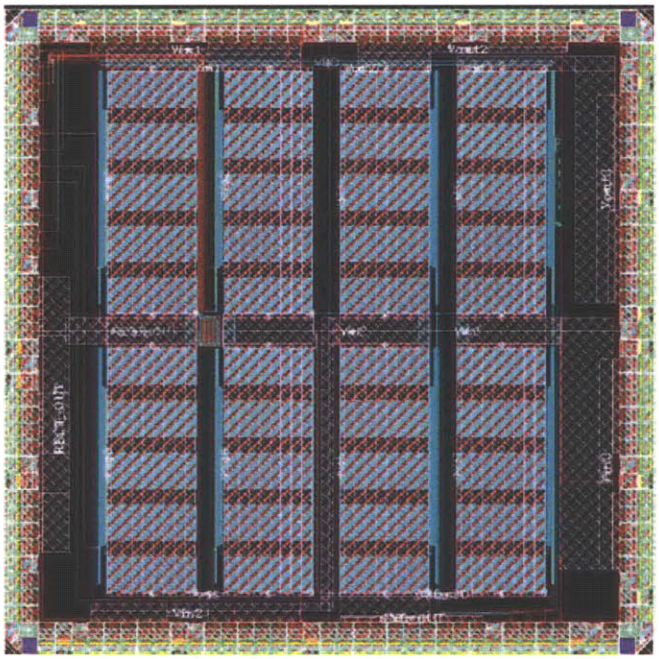

Figure 3-4: Power transistor chip layout in CMOS 0.18 um process. The size of the chip is 3 mm x 3mm while the bare die mass is 0.0126 g if assuming the chip thickness to be 600 μm.

three phase converter with three chips. The full layout of eight transistors can be seen in Figure 3-4. The eight large blocks taking up the majority of the layout space are the power MOSFETs. Since power MOSFETs are much larger than ordinary MOSFETs in CMOS process, design issues such as pattern density and antenna effect have to be taken with special care. Certain layout techniques have also been employed to decrease the DC resistance of the circuit and to increase the testability of the circuit.

Power MOSFET

The two most prominent issues that arrise from laying out power MOSFETs in standard CMOS process are the interconnect series resistance and the pattern density. In order to minimize the series resistance, metal layers two to five, connected by vias, have been used to form parallel connections within and in between MOSFETs.

For CMOS processes, the pattern density rule checks to see if the density of a certain layer is within the minimum and maximum limits defined by the chip manu-

facturer. These limits are set such that the physical semiconductor structure of the circuit is robust enough that it does not collapse or misalign. The high density usage of layers of the power MOSFET would exceed the maximum density limits defined by the pattern density rules. Therefore, each MOSFET is separated into five parts to decrease the layer densities. This can be seen in Figure 3-4. The five parts are represented as blocks with light blue background and red diagonal lines. They are interconnected by metal layers shown in red. To further decrease the series resistance in the power path, we connected 12 pads in parallel for each input and output port.

Chip for testing

Once the chip is fabricated and packaged, the test engineer would have to settle with the given pins to understand the dynamics of the circuit. In addition, misdesigned circuits could also compromise the operation of the entire chip. Therefore, it is important to create output testing ports at important nodes for debugging, and also to provide bypass routes such that malfunctioning circuits can be replaced by off-chip circuits. Since the goal of this chip is to test the performance of the basic converter components and provide test results useful for designing the second generation chip, the testability is extremely important. In addition, we put in bypass circuits that bypass the full bridge rectifier and gate driver so that the boost converter and the power MOSFETs can be tested independently.

3.3 Inductor Design

Beyond the desired inductance and stored energy, the two major parameters of an inductor are its size and operating frequency. Trading these two parameters is a optimization process of finding the most efficient solution with the given physical limitations, design specifications and tradeoffs. As we recall from Section 2.1, the mass of the harvesting system has to be less than 1 g and fit in a tent-shaped physical space. These physical limitations set the upper boundaries of the physical and inductive size of the inductor. Since we will be requiring 4 inductors for the two stage

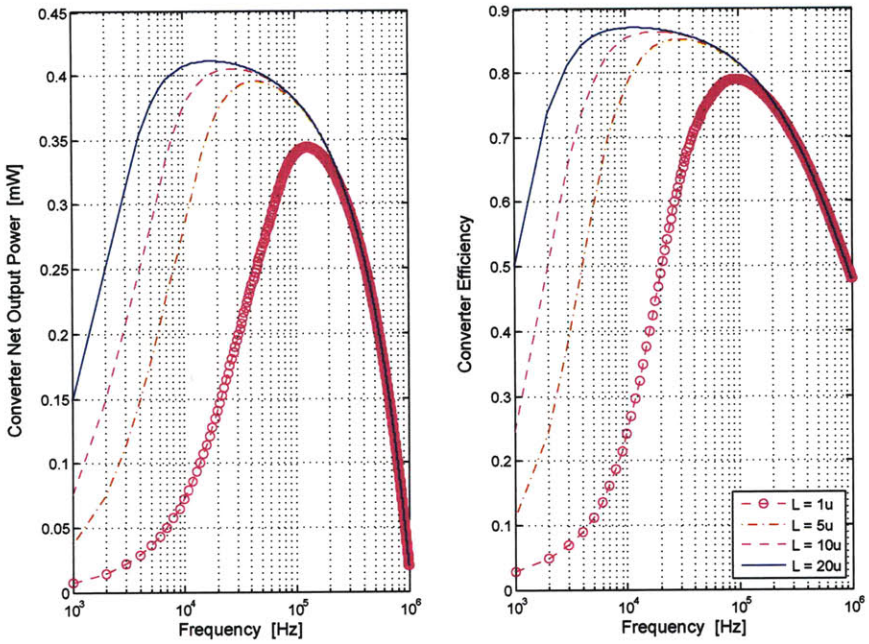

Figure 3-5: Inductor size and operation frequency effect on one phase of the first-stage boost converter output power and efficiency.

boost converter, we will allocate approximately 0.1 g for each inductor. A survey of commercial inductors was conducted to find the inductor size range under the given weight limitation. The largest possible inductor was determined to be around 20 μH.

With the inductor size upper bound determined, the next step would be determining the optimal operating frequency for all possible inductor sizes. Here we define the optimal frequency to be the frequency at which the converter can deliver the most power to the output since we hope to deliver as much power as possible to the flight control system. We then apply a frequency sweep on various inductor sizes. Corresponding converter output power and efficiencies are shown in Figure 3-5. This simulation was done together with the transistor optimization.

The output power and efficiencies in Figure 3-5 not only take the power loss in the energy path into account, but also the switching losses due to switch capacitance. The concave downward shape of the curves (neglecting the curve at lower frequencies) are due to two pulling factors. At higher frequencies, the converter can pump more power to the output. However, since the switching loss CV^2f is proportional to the switching

frequency, the switching loss also increases linearly with frequency. Therefore, there exists an operating frequency which the converter can deliver the maximum amount of power for each inductor size.

From Figure 3-5, we can see the advantages in having a inductor with a larger inductance as it results in higher converter output power and efficiency. The performance increase is most significant when the inductor size is changed from 1μH to 5μH while the performance improvement slows down when increasing the inductor size from 10μH to 20μH. In order to make our converter as light as possible while not giving up significant amount of output power capabilities in exchange we chose our first pass inductor size to be 10μH. As a result, we trade less than 3% of power out for a mass reduction as large as 50%.

In the search of providing a 10μH inductor for the converter, we pursued three possible directions. The first was to buy commercial or tailor-made inductors that satisfied our specifications. Unfortunately we were unable to find any suitable inductors that had a mass of 0.1 grams, inductance of 10μH, and DC resistance on the order of 10 milli-ohms. The second path we took was investigating the possibility of using the harvester's own electromagnetic coil as the inductor. If possible, this would be an excellent solution since it decreases the number of inductors required from four to one. The total mass of the converter would be greatly reduced as each inductor weighs an estimate of 0.1 grams. With careful measurement, the inductance for each phase of the coil was on average 50 nH, 20 times lower than our desired of 10 μH and thus too small to deliver sufficient power. Due to the fact that no commercial inductors met our specifications and that the harvester coil inductance was too small, we decided to design and build our own inductors.

With the support of the Perreault group, we were able to have access to an inductor optimization program implemented in MATLAB. The program, which can be found in Appendix A.3, calculates the DC and AC power losses of the inductor and takes the coil and core dimensions into account. By using the inductor optimization program, an inductor power loss versus mass tradeoff curve was generated as shown in Figure 3-6. We can see from the figure that the inductor power loss varies from 0.015 mW

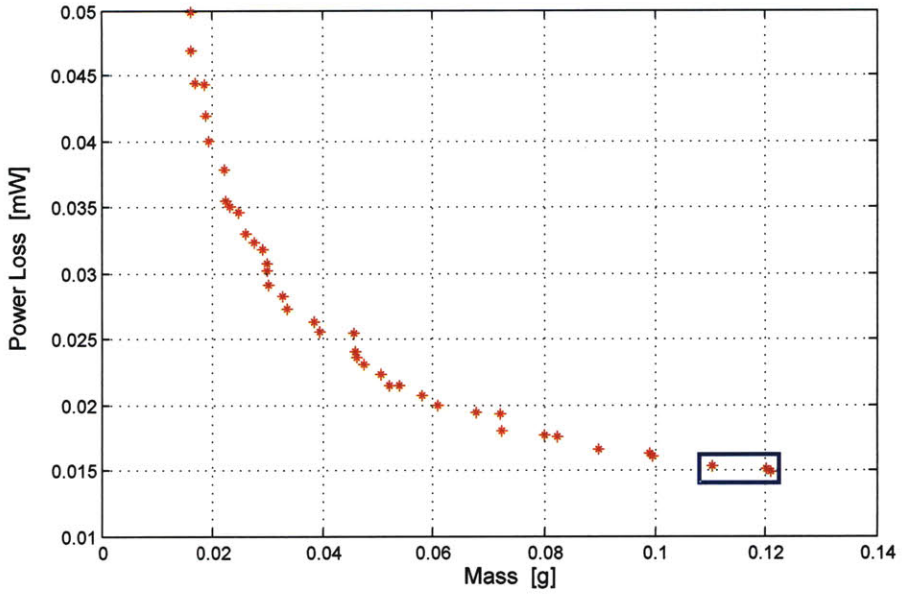

Figure 3-6: Power loss versus physical mass tradeoff of a 10 μH inductor operating at I_{dc} = 65 mA and f = 100 kHz.

Core Model	**Overall**		**Core Dimensions**				
	Mass	Power Loss	Height	Din	Dout	Coil Diameter (AWG)	Turns
TC3.1/1.8/2	0.12	0.016	2.03	1.78	3.05	0.54(23.5)	5
TC3.4/1.8/1.3	0.11	0.015	1.27	1.78	3.43	0.54(23.5)	5
	$[g]$	$[mW]$	$[mm]$	$[mm]$	$[mm]$	$[mm]$	♯

Table 3.2: Optimal design parameters of a 10 μH inductor with a mass near 0.1 g.

to 0.05 mW, which is respectively 1.5% to 5% of the total generated power, assuming that 1 mW of power is scavenged by the harvester. If we take the number of inductors into account, the total power loss caused by inductors would be 6% to 20% of the total power. Due to the large inductive losses, we chose the designs in the lower right corner box of Figure 3-6 in order to minimize the power loss while pushing the mass to the upper limit.

In order to validate the designs and the optimization process, we chose two inductor cores provided by Ferroxcube[2] that had similar dimensions to our design. Design details of the two designs are listed in Table 3.2.

[2]www.ferroxcube.com/

3.4 Discrete Circuit Verification

During the 3 month fabrication time of our designed integrated circuit, we implement our circuit with discrete components to verify the functionality, power throughput and efficiency of our topology. In addition, it also gives us the flexibility of testing and developing a good pulse-width modulation (PWM) control scheme and on/off strategy. Power MOSFETs and inductors with similar electronic characteristics to our design were chosen. Our greatest focus was the series resistance in the power path.

For the power MOSFET, we chose the Si4838DY N-Channel MOSFET provided by Vishay[3]. It displays an on-state resistance of 3 mΩ when the gate to source voltage is 4.5 V. This on-state resistance is comparable to the 1 mΩ resistance of our integrated version simulated in Cadence. As we recall, the output resistance of the harvester is 0.1 Ω, therefore, the low on-state resistance of the Si4838DY makes it an ideal choice for conducting discrete circuit verification experiments. The gate to source voltage is comparably higher than the 1 volt gate to source voltage of our MOSFETs fabricated in 0.18 μm CMOS process. This leads to a larger gate switching loss which is proportional to V^2. However, since the main focus of our discrete circuit analysis is on the power path, the gate power losses will not be taken into account.

In Figure 3-7, we can see the entire boost converter implemented on a printed circuit board by Dave Otten. The four large blocks on the top row of the layout are the four 10 μH inductors while the eight pin blocks laid on the second and third rows are the power MOSFETs. In addition to these two major discrete components, a micro-processor is put onto the board to provide programmable control abilities. It is the flat square shaped component on the bottom of the board.

In order to predict the optimal duty cycle and hence develop a look up table for the feedback control, an accurate model for the discrete circuit is needed. Specifically speaking, we need good device models that characterize the MOSFET and inductor well. The MOSFET model we chose can be found in Figure 3-8(b). The transistor

[3]www.vishay.com

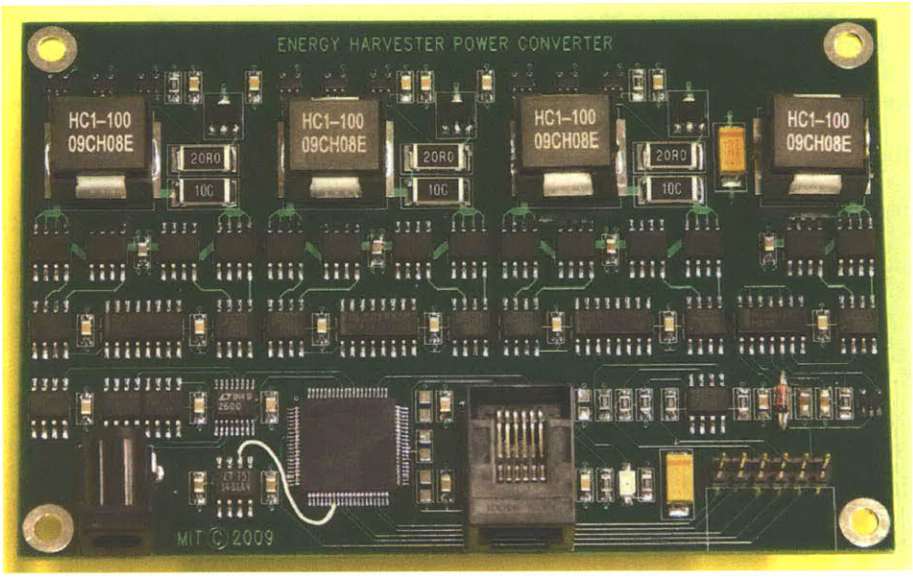

Figure 3-7: Discrete 2-stage boost converter. This circuit was built by Dave Otten and verified that our 2-stage boost converter topology works.

model includes the gate resistance, R_G, the gate capacitances, C_{GD} and C_{GS}, the output capacitance, C_{DS}, the body diode, D, and the on-state resistance, R_{ON}. These parameters were taken from its data sheet and fine tuned such that model can more accurately represent the experiment settings. The inductor model on the other hand takes the DC resistance of the inductor, R_L, into account. These parasitic parameters are shown in Table 3.3. With accurate device models of the MOSFET and inductor, we simulated the discrete boost converter, which is shown in Figure 3-8(a), in Cadence and compared it with experimental results. The experiment conditions were at $V_i =$ 14 mV and $V_o = 50$ mV.

Finding the optimal duty cycle for different input voltages is critical for our boost converter since V_i is a time-varying voltage source with an RMS value approximately 14 mV. In Figure 3-9, we see the output power versus duty cycle plot with comparisons between the experiment and the simulation. As we can see from the figure, the experiment and the simulation output power match nicely over the entire duty cycle range which generates delivers positive power to the output. This indicates that the device models can nicely predict the performances of the discrete circuit, and therefore

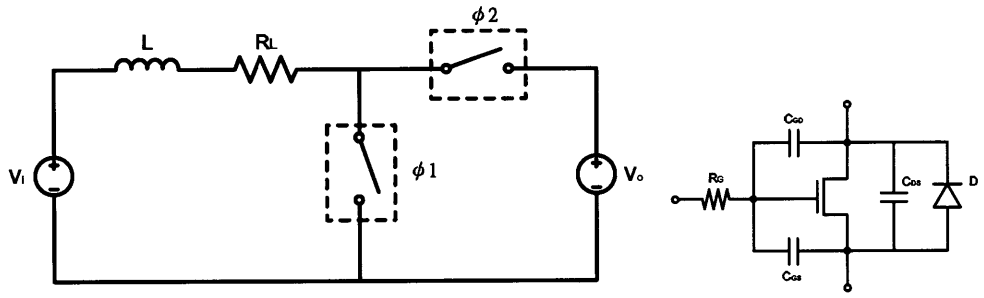

(a) First stage boost conveter schematic (b) Transistor model

Figure 3-8: First stage boost conveter model

Parasitic Parameters						
R_L	R_{ON}	R_G	C_{GS}	C_{GD}	C_{DS}	V_D
0.0057	0.0025	4	3	5	5	0.6
[Ω]			nF			[V]

Table 3.3: Discrete switch model parameters.

become a reliable tool of finding the optimal duty cycle for various input voltages.

In Figure 3-10 an optimal duty cycle versus input voltage plot generated by our simulation is shown. This provides us with a quick first pass look-up table to find the optimal duty cycle. Even though experimental results of our chip are not availble at this moment, we are confident from the preliminary experiments and the good matching between the experiment and simulation shown in Figure 3-10 that future experiments will verify this optimal duty cycle plot.

3.5 Chapter Summary

In this chapter, we first addressed the various challenges of the power electronics and then visited various possible circuit topologies. The 2-stage boost converter was chosen as the final design due to its good properties for high ratio boost conversion. MATLAB and Cadence circuit simulations were then applied to aid the optimization of the design. The power transistors are currently being fabricated in National Semiconductor's 0.18 μm CMOS process. Experimental data on the chip are unavailable at the moment, but a discrete circuit version of the circuit was built and has success-

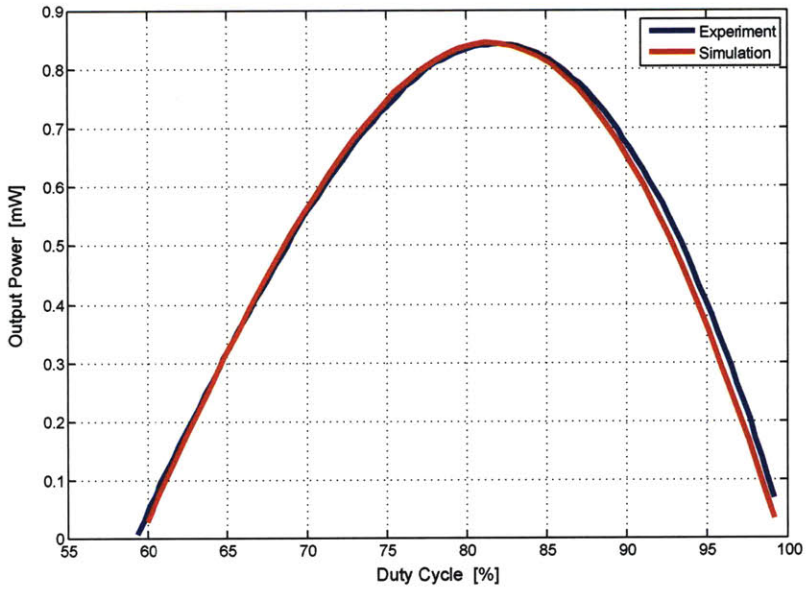

Figure 3-9: Comparison between experimental and simulation output power of first stage boost converter

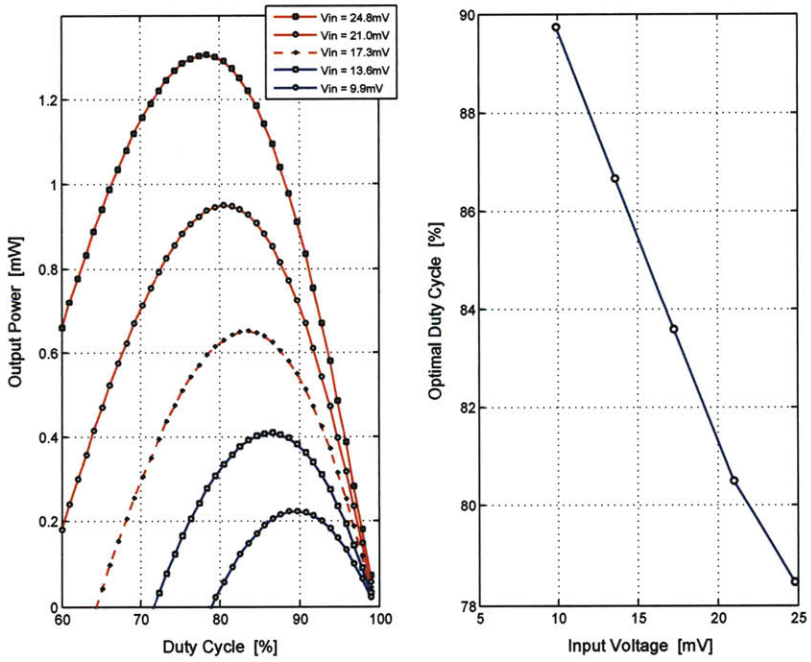

Figure 3-10: Boost converter optimal duty cycle for different input voltages

fully verified the behavior of our topology. A good model for the dicrete components was also developed for control scheme simulations.

Chapter 4

Summary, Conclusion, and Future Work

Having gone through the entire process of exploring a electromagnetic vibration energy harvesting topology, from fundamental circuit theory to MATLAB optimizations and system prototyping, one might wonder what further improvements can be made to the harvesting system. Before answering that question, each chapter will first be summarized briefly and the important conclusions will be highlighted. Numerous suggestions on future improvements to the system follow.

4.1 Summary

Chapter 1 introduced the concept of energy harvesting and provided the background of the HI-MEMS program. Previous research in vibration energy harvesting were also revisited as a comparison to our work. The normalized power $P_n = P/P_{MAX}$ [2] measures how close the performance of a specific device comes to the optimum level. Both frequency and the mass of the proof-mass are normalized in the calculation. From the harvesters reviewed in [2] and the latest harvesters presented at PowerMEMS 2009, all harvesters have a P_n smaller than 0.2 while the harvester reported in this thesis has a $P_n = 0.36$ at 25 Hz. The major research challenges of this project were also discussed in Chapter 1. For the energy harvester, the most challenging part was to

deliver 1-mW of power with the limited physical space and mass allowed. As we can see in Chapter 2, the tradeoff between low mass and high power is significant. On the other hand, the power electronics faced the issue of rectifying and converting the low output AC voltage of the harvester to a high DC voltage. In addition, the low output resistance of the harvester made the design of the power electronics even more challenging. Finally, at the end of the chapter, a high level system overview of the harvesting system was given.

Chapter 2 focused on the design of the electromechanical energy harvester which performs the conversion between mechanical and electrical energy. Possible energy sources and harvesting methods were investigated in this chapter. Once finalizing the approach, magnetic and mcechanical analyses were performed to form a model for our electromagnetic energy harvester. This model was used as the core of a optimization process of finding the design that could generate the most power while weighing the least. Two specific designs were chosen from the optimization results and fabricated. With two generations of iterations, a harvester structure built with ABS plastic has been developed and successfully delivered more than 1.7 mW of power with a mass of 1.28 g. A third generation design achieving 0.99 mW and 0.93 g with the same input vibration but smaller harvester vibration amplitude has been produced since the writing of this thesis.

In Chapter 3, different possible circuit topologies were first visited. In order to make the transistor resistances small relative to the output resistance of the harvester, the transistor channel width were designed to be extremely large, hence making the gate capacitance of the transistor large. The large transistor sizes limited the switching frequency to tens of kilo-hertz such that the power loss due to dynamic switching is within a few percent of the output power. With the operation frequency range decided, we decided to take a multi-stage tapped boost converter approach. Our topology was simulated in Cadence and optimizaed in MATLAB. The power MOSFETs of the converter are fabricated in 0.18 μm CMOS process while the inductors are self made toroid inductors. The circuit topology was verified with discrete circuit components.

4.2 Conclusions

There were three major bottleknecks during the lifetime of this thesis - the mass limit, the inductor size and the transistor losses. The moth payload limit of 0.6 - 1 g made the harvester design extremely challenging. From the beginning of the project, we had to make the tradeoff between mass and power. Our simulation code took the design constraints of the flexible PCB and the magnetic core dimensions into account and generated an optimal design curve between power and mass. From our experiments in Sections 2.4.1 and 2.4.2, our magnetic model, circuit model and FEA simulations accurately predicted the output voltages and optimal load of the harvester. However, our mass predictions were inaccurate since we did not take the mass of supporting structure into account. The supporting structure mass issue was extremely challenging, but with clever ABS plastic designs by Frank Yaul, we were able to reduce the harvester mass near the moth payload limit. In summary, the harvester reported in this thesis has a total mass of 1.28 g with a spring mass of 322 mg, flexible PCB mass of 288 mg and proof-mass mass of 669 mg. The proof-mass mass combines six magnets at 240 mg, two cores at 180 mg and the plastic carrier at 249 mg.

The inductor design and transistor losses are also major challenges that we attempted to address during the process of this thesis but did not have time to verify our simulations in experiment. A prototype of the 10 μH inductors we designed was made and had a Q of 38 and DC resistance of 11 mΩ, which were both close to the simulation. However, the AC losses were not measured and remain to be determined in the future. Lastly, the transistor losses inside the chip were decreased by using multiple metal layers. The testing of the transistors is also one of the future works.

4.3 Future Improvements

This is an on-going project that could last until the end of 2010. The ultimate goal is to let the entire energy harvesting system, which includes the harvester itself and

the power electronics, become flyable on the hawk moth. Between the project goal and our current status, there still remains plenty of opportunities for improvement. Let us take a bottom up approach starting with the harvester.

For the harvester, the next step would be flying the harvester with a resistive load on a moth. However, this requires further reducing the total mass of the harvester which could be achieved by carefully trimming down the ABS structure and implementing the structure with carbon fiber. The flight experiment would not only prove the flyability of the harvester but also prove that the moth thorax vibration can indeed generate 1 mW of power into a resistive load, which can be estimated by the vibration amplitude of the harvester. Now let us shift our focus to the power electronics.

Once the chip comes back, testing of the power MOSFETs characteristics and the strong-ARM comparator's performances would be the first task. In the mean time, PWM control schemes for the power electronics will be tested on the discrete boost converter and then implemented on the next generation integrated circuit. However, we would like to take an overall view of the energy harvesting system before taping out the second chip. Ulitmately, we hope to have all the power electronics except the inductors integrated into one chip.

In this thesis, we first optimized the harvester and then designed the power electronics with the given test results from the energy harvester. However, an overall optimization of the entire system was never in place. Now with experimental results and better understanding of the various challenges, it makes most sense to consider the entire energy harvesting system when conducting the optimization. As we have seen while designing the power electronics, boosting a voltage from 14 mV to 1 V requires multi-stages and would require multiple off chip inductors, which are extremely heavy compared to the energy harvester magnetic core. Therefore, giving more mass budget to the harvester while gaining a higher output voltage may reduce the number of stages required in the power electronics and hence reduce the mass of the entire system. Another possibility is utilizing the inductance of the harvester coils such that off chip inductors can be eliminated. In short, a full system optimization process

would be required in order to achieve our goal of a flying energy harvesting system.

4.4 Final Words

The HI-MEMS program is no doubt one of the most crazy, science fiction projects I have ever worked on. We may or may not see flying moths being remote controlled by human in our lives, but the engineering breakthroughs in radio communication, bio-MEMS, insect flight modeling, and energy harvesting may have a faster impact on our lives than expected. The subject of energy harvesting presents itself as an uniquely challenging field of research. Maybe one day, in the hallways of MIT or in the subway stations or on the sidewalks of Times Square, the vibration energy would be large enough such that low power illumination devices may be used. People might acutally help save energy ... by just walking by.

Appendix A

MATLAB Codes

A.1 Harvester Optimization

The harvester optimization code is extremely computational expensive and time consuming. The following code was broken down into 10 parts and ran in parallel on Athena clusters for six to seven hours each time. This is due to the fact that 1500 sets of parameters had to be run for each of the ten run sets and for each set of parameter, the process of satisfying all the internal damping factor equations requires a lot of time. The run-time of this code can definitely be decreased by the aid of MATLAB profiler and by replacing FOR loops into vector calculations.

```
% ------------------------------
% HARVESTER OPTIMIZATION CODE
% ------------------------------

clear all
close all

load B_table.mat
B_table_x = 0.2 : 0.1 : 0.8;
B_table_y = 0 : 1 : 10;

%% CONSTANTS

CM = 8000;                    % core mass density [kg/m3]
```

```
MM = 7500;                      % magnet mass density [kg/m3]
WM = 8960;                      % winding mass density [kg/m3]
CC = 6e7;                       % Coil conductivity [S/m]
Y = 1.146e-3;                   % Moth vibration amplitude [m]
NT = 2000;                      % Number of time steps per cycle
NP = 3;                         % Number of Phases
E = 45*pi/180;                  % Coil end turn angle [rad]
G = 100e-6 + 6.35e-6;           % Physical air gap + Singular Cover [m]
J = 100e-6;                     % Iron core thickness [m]
T = 35e-6;                      % Coil layer thickness [m]
KW = 8.89e-5;                   % Kerf width [m]
CT = 25.4e-6;                   % Cover Thickness [m]
AX = 5e-3;                      % Max motion amplitude [m]
W = 2*pi*25;                    % motion frequency [rad/s]
counter = 0;                    % counter for result table


%% DESIGN SWEEP

for ML = 4.5e-3 : 0.5e-3 : 10e-3            % Magnet Length [m]
  for MW = 1e-3 : 0.1e-3 : 3e-3             % Magnet Width [m]
    for MT = 0.3e-3 : 0.02e-3 : 0.5e-3      % Magnet Thickness [m]
      for NM = 1 : 5                        % Number of Magnets

        % ------------------------------------------
        % COMPUTE MAXIMUM TURN PER CELL PER PHASE
        % ------------------------------------------

        NC_max = floor( MW/1.651e-4 );      % MAX turns / cell
                                            % 1.651e-4 = min(Kerf+Trace)
        NC_max = floor( NC_max/NP );        % MAX turns / phase

        for NC = 1:NC_max                   % Number of Coils
          for NCell = 1:5                   % Number of Cells
            for Layer = 1:3                 % Number of Coil Layers

              % ----------------------
              % COMPUTE WINDING WIDTH
              % ----------------------

              WW = [(MW)-(NC*NP*KW)]/NC/NP;     % Winding Width

              % ----------------
              % COMPUTE MASSES
              % ----------------
```

```
% WMass: Winding   MMass: Magnet   CMass: Core   TMass: Total
WMass = [ML + MW/sin(E)/cos(E)]*2*NC*NCell*Layer*T*WW*NP*WM;
MMass = NM*MT*MW*ML*MM;
CMass = (2*J+MT+2*G+T*Layer)*J*MW*NM + (ML+MW*tan(E))*J*MW*NM * 2;
CMass = CMass * CM;
CoverMass = CT * (ML+MW*tan(E)) * (MW*NM) * Layer;
CoverMass = CoverMass * 1000;
TMass = WMass + MMass + CMass + CoverMass;

% IF Total Mass > 0.2g -> STOP sweep
if ( TMass < 0.143e-3 || TMass > 0.5e-3)
   break
end

% ------------------------
% INTERPOLATE MAGNETIC FLUX
% ------------------------

P_P = MT + 2*G + (T+CT)*Layer;      % Core Plate to Plate air gap
B_A = MT / P_P;                     % Mag Thickness / Iron Core P2P
C_A = MW / P_P;                     % Mag Width / Iron Core P2P

if (B_A > 0.8 && C_A < 10)
    B = interp1(B_table_y, B_table(:,7), C_A);
elseif (C_A > 10 && B_A < 0.8)
    B = interp1(B_table_x, B_table(10,:), B_A);
elseif (B_A > 0.8 && C_A > 10)
    B = 0.99;
else
    B = interp2(B_table_x, B_table_y, B_table, B_A, C_A);
end

% ------------------------
% COMPUTE FLUX LINKAGE ARRAY
% ------------------------

F = zeros(NM+NCell+1,1);                    % flux linkage vector

for N1 = 0:NM-1                             % for all magnets
  for N2 = 0:NCell-1                        % for all coils
    M = N1+N2+2;                            % peak position
    F(M) = F(M) + ((-1)^(N1+N2))*B*MW*ML;   % flux linkage peak
  end                                       % continue
end                                         % continue
```

```
F = F * Layer;

% ------------------------------------
% PAD FLUX LINKAGE AT ENDS IF NEEDED
% ------------------------------------

X = zeros(ceil(max(0,AX/MW-(NM+NCell)/2)),1);      % pole padding
F = [X;F;X];                                       % flux linkage
Span = size(F,1)-1;

% ---------------------------------
% COMPUTER SINGLE COIL RESISTANCE
% ---------------------------------

R = [ML + MW/sin(E)/cos(E)]*2*NC*NCell*Layer;      % coil length
R = R/T/WW/CC;                                     % resistance

% ------------------------------
% BEGIN MOTION AMPLITUDE LOOP
% ------------------------------

ASave = [];                                        % Amplitude save vector
PSave = [];                                        % Power save vector
RRSave = [];                                       % Resistor ratio vector

for A = (1:100)*AX/100;                            % Sweep all amplitudes

   % ---------------------------
   % COMPUTE VOLTAGE AND POWER
   % ---------------------------

   X = A*sin(2*pi*(0:NT)'/NT);                     % X(t) Disp. at times
   U = A*W*cos(2*pi*(0:NT)'/NT);                   % U(t) Velocity at times
   V = zeros(NT+1,1);                              % V(t) Voltage at times
   Z = X/MW + Span/2;                              % Index in flux array
   Z = (F(1+ceil(Z))-F(1+floor(Z)))/MW;            % Spatial flux derivative
   V = Z.*U;                                       % Temporal flux derivative

   % ---------------------------------
   % COMPUTE INTERNAL DAMPING FACTOR
   % ---------------------------------

   B_int = 3.6787 * (CMass+MMass);                 % Internal Damping Factor
                                                   % 3.6787 found from exp.
```

```
   % ------------------------------------
   B_x = (MMass+CMass)*W*Y/AX - B_int;      % External Damping Factor
   % ------------------------------------

   Z_avg = mean(Z.^2);
   RR = Z_avg/R/B_x-1;                  % Ratio of Internal to Load R

   if ( RR < 0 )
        ASave = [];
        PSave = [];
        RRSave = [];
        Recal_Sig = 1;
        break
   end

   P = NP*(V.*V)/(R*(1+RR));      % Converted electrical power
   PAvg = mean(P(2:NT+1));        % Compute mean power
   ASave = [ASave;A];             % Save amplitude
   PSave = [PSave;PAvg];          % Save average power
   RRSave = [RRSave;RR];

end

if (Recal_Sig == 1)
for A = (1:100)*AX/100;           % Sweep all amplitudes

   % ---------------------------
   % COMPUTE VOLTAGE AND POWER
   % ---------------------------

   X = A*sin(2*pi*(0:NT)'/NT);
   U = A*W*cos(2*pi*(0:NT)'/NT);
   V = zeros(NT+1,1);
   Z = X/MW + Span/2;
   Z = (F(1+ceil(Z))-F(1+floor(Z)))/MW;
   V = Z.*U;

   % ------------------------------------
   % COMPUTE INTERNAL DAMPING FACTOR
   % ------------------------------------

   B_int = 3.6787 * (CMass+MMass);

   % ----------
   B_x = B_int;
```

```
    % ----------

    Z_avg = mean(Z.^2);
    RR = (Z_avg/R/B_x)-1;

    P = NP*(V.*V)/(R*(1+RR));
    PAvg = mean(P(2:NT+1));

    ASave = [ASave;A];
    PSave = [PSave;PAvg];
    RRSave = [RRSave;RR];

end
end

Recal_Sig = 0;

if (isempty(RRSave))
    break
end

% ---------------------------------
% DETERMINE AMPLITUDE AND POWER
% ---------------------------------

QSave = MMass*ASave*Y*W*W*W/2;          % mechanical input power
[Index,Index] = min((PSave-QSave).^2);  % intersection index
Amp = ASave(Index);
RR = RRSave(Index);

% ------------------------------------------------
% RECOMPUTE VOLTAGE AND POWER AT INTERSECTION
% ------------------------------------------------

X = ASave(Index)*sin(2*pi*(0:NT)'/NT);
U = ASave(Index)*W*cos(2*pi*(0:NT)'/NT);
V = zeros(NT+1,1);

Z = X/MW + Span/2;
Z = (F(1+ceil(Z))-F(1+floor(Z)))/MW;
V = Z.*U;

P = (RR/(1+RR))*NP*(V.*V)/(NC*R*(1+RR));
P_OP = PSave(Index)*1000*RR/(1+RR);
```

```
break_sig = 0;
for counter2 = 1 : counter
    if ( P_OP < sort(counter,1) && TMass*1000 > sort(counter,7) )
        break_sig = 1;
        break
    end
end

if ( break_sig == 1 )
    break
end

P_VIB = PSave(Index)*1000;                          % Vib Power [mW]
X_VIB = ASave(Index)*1000;                          % Vib Amplitude [mm]
TMass_INV = 0.1/TMass/1000;                         % Inv. TMass [0.1/g]
V_MAX = max(V*1000*RR/(1+RR));                      % MAX Vout [mV]
V_MEAN = mean(abs(V*1000*RR/(1+RR)));               % Mean |Vout| [mV]
CF = WW/(WW+KW);                                    % Copper Fraction
P_B_int = 0.5*B_int*W^2*ASave(Index)^2*1000;        % Ploss B_int [mW]

counter = counter + 1;
sort(counter,1) = P_OP;          % Output Power [mW]
sort(counter,2) = TMass_INV;     % Inverse of Total Mass [0.1/g]
sort(counter,3) = V_MAX;         % Maximum output voltage [mV]
sort(counter,4) = V_MEAN;        % Mean output voltage [mV]
sort(counter,5) = P_VIB;         % Vibration Power [mW]
sort(counter,6) = X_VIB;         % Vibration Amplitude [mm]
sort(counter,7) = TMass*1000;    % Total Mass [g]
sort(counter,8) = CMass*1000;    % Core Mass [g]
sort(counter,9) = MMass*1000;    % Magnet Mass [g]
sort(counter,10) = WMass*1000;   % Winding Mass [g]
sort(counter,11) = RR;           % Resistor Matching Ratio
sort(counter,12) = MT*1000;      % Magnet Thickness [mm]
sort(counter,13) = MW*1000;      % Magnet Width [mm]
sort(counter,14) = ML*1000;      % Magnet Length [mm]
sort(counter,15) = NP;           % # phases
sort(counter,16) = NCell;        % # cells
sort(counter,17) = NM;           % # magnets
sort(counter,18) = NC;           % # coils / phase
sort(counter,19) = Layer;        % # layers
sort(counter,20) = WW;           % winding width
sort(counter,21) = B;            % magnetic flux [T]
sort(counter,22) = CF;           % copper fraction
sort(counter,23) = B_int;        % internal damping factor
sort(counter,24) = P_B_int;      % Ploss internal damping [mW]
```

```
                sort(counter,25) = R;              % resistance [ohm]

            end
          end
        end
      end
    end
  end
end
```

A.2 Two Stage Tapped Inductor Boost Converter Optimization

The first stage optimization code for the two stage tapped inductor boost converter. The concept behind the code can be found in Section 3.2.1. The second stage optimization code can be obtained by simply modifying the input and output voltage conditions of its first stage counterpart. Solving differential equations can be time consuming in MATLAB especially for a optimization sweep. Therefore, we pre-solved the differential equations given in Section 3.2.1, and plugged the parameters directly into the transient current functions $f3$ and $f4$. In addition, the current squares were also calculated in advance as functions $f1$ and $f2$.

```
% ------------------------------------------------------------------------
% OPTIMIZATION FOR 1st STAGE OF THE 2 STAGE TAPPED INDUCTOR BOOST CONVERTER
% ------------------------------------------------------------------------

clear all
close all

% ----------
% Constants
% ----------

Rsp = 0.612;                    % Channel Width x Ron Constant
Csp = 0.662;                    % Cap / W
counter = 0;                    % counter for result table
RH = 0.1;                       % Harvester Output Res. [Ohms]
```

```
tol = 1e-19;                                % Quad Function Tolerence

% ------------------------
% FIXED DESIGN PARAMETERS
% ------------------------

V1 = 14e-3;                                 % Harvester Output RMS Voltage [V]
W1 = 100;                                   % Switch 1 Channel Width
W2 = 100;                                   % Switch 2 Channel Width
Rs = 0.01;                                  % Inductor Series Resistance [Ohms]
Vg = 1.8;                                   % Switch Gate Voltage
Ron1 = 0.612/W1;                            % Switch 1 ON Res. [Ohms]
Ron2 = 0.612/W2;                            % Switch 2 ON Res. [Ohms]
Cgs1 = W1*Csp*1e-12;                        % Switch 1 Cgs [F]
Cgs2 = W2*Csp*1e-12;                        % Switch 2 Cgs [F]

% ----------------
% PARAMETER SWEEP
% ----------------

for f = 10e3 : 10e3 : 200e3                 % Frequency Sweep
    for D = 0.8 : 0.01 : 0.99               % Duty Cycle Sweep
        for L1 = 1e-6 : 1e-6 : 20e-6        % Primary Inductor Sweep
            for V0 = 30e-3 : 10e-3 : 300e-3 % 1st Stage Output Voltage Sweep
                for N = [0 1 2]             % Prim. to Sec. Ind. ratio Sweep

                    T = 1/f;
                    P1 = D*T;               % Switch 1 ON time [s]
                    P2 = (1-D)*T;           % Switch 2 ON time [s]
                    L2 = (N+1)^2*L1;        % Equi. Ind. (S1 OFF) [H]
                    R1 = Ron1 + Rs/(N+1) + RH;  % Equi. Res. (S1 ON) [Ohms]
                    R2 = Ron2 + Rs + RH;    % Equi. Res. (S1 OFF) [Ohms]
                    V2 = V1 - V0;           % (Vin - Vout) [V]

                    % ------------------------------------
                    % FIND WHEN CURRENT 2 BECOMES ZERO
                    % ------------------------------------

                    stop = I2decayTime (N,D,P1,P2,L1,L2,R1,R2,V1,V2,0,100);

                    % ------------------------------------------------------------
                    % FIND INTEGRALS OF CURRENT SQUARE FOR POWER COMPUTATION
                    % ------------------------------------------------------------

                    intI1square = f1(N,D,P1,P2,L1,L2,R1,R2,V1,V2,0,P1,tol);
```

```
intI2square = f2(N,D,P1,P2,L1,L2,R1,R2,V1,V2,0,stop,tol);
intI2 = f3(N,D,P1,P2,L1,L2,R1,R2,V1,V2,0,stop,tol);
intI1 = f4(N,D,P1,P2,L1,L2,R1,R2,V1,V2,0,P1,tol);

% ----------------
% CALCULATE POWER
% ----------------

E1 = intI1square * (R1-RH);              % Phi1 Energy Loss
E2 = intI2square * (R2-RH);              % Phi2 Energy Loss
if E1 < 0 || E2 < 0
    break
end
ECap = Cgs1 * Vg^2 + Cgs2 * (Vg-VO)^2;  % Switch Cgate Loss
Eh = V1 * (intI1+intI2);                 % Harvester Pout
Erh = (intI1square + intI2square)*RH;    % RH Loss Energy
Eo = VO * intI2;                         % Eout per Cycle
Eff = Eo / (Eo+E1+E2+ECap);              % Efficiency

Prh = Erh/T*1e3;                         % RH Loss Power
Ph = Eh/T*1e3;                           % Harvester Pout
Pin = Ph - Prh;                          % Converter Pin
Pout = Eo/T*1e3;                         % Converter Pout
Ploss1 = E1/T*1e3;
Ploss2 = E2/T*1e3;
PCap = ECap/T*1e3;
PNET = Pout - PCap;

% ---------------
% DESIGN FILTER
% ---------------

if Pout > 0.4  && L2 < 50e-6             % Pout > 0.4 mW
    counter = counter + 1;
    sort(counter,1) = Eff;               % Converter Efficiency
    sort(counter,2) = VO*1e3;            % 1st Stage Vout [mV]
    sort(counter,3) = PNET;              % Power Input [mW]
    sort(counter,4) = Pin;               % Power Out [mW]
    sort(counter,5) = Ploss1;            % Ploss in cycle 1 [mW]
    sort(counter,6) = Ploss2;            % Ploss in cycle 2 [mW]
    sort(counter,7) = PCap;              % Cap Loss [mW]
    sort(counter,8) = f/1e3;             % Frequency [kHz]
    sort(counter,9) = L2*1e6;            % Inductor Size [uH]
    sort(counter,10) = N;                % Tap Inductor Ratio N
    sort(counter,11) = D;                % Duty Cycle
```

```
                    end

                end
            end
        end
    end
end


% ------------------------------------------
% CALCULATES INTEGRAL OF CURRENT 1 SQUARE
% ------------------------------------------

function f1 = current1 (N,D,P1,P2,L1,L2,R1,R2,V1,V2,start,stop,tol)

order=0;

f1 = quad(@intI1square,start,stop,tol);

    function f1 = intI1square(t);
        f1 = ((V1+exp(-R1/L1*t)*(-R1*N*V2+R1*N*exp(-R2/L2*P2)*V2-R1*V2+R1*exp(-R2/↩
            L2*P2)*V2-exp(-R2/L2*P2)*R2*V1+R2*V1)/(-1+exp(-R1/L1*P1)*exp(-R2/L2*P2)↩
            )/R2)/R1).^2;
    end
end


% ------------------------------------------
% CALCULATES INTEGRAL OF CURRENT 2 SQUARE
% ------------------------------------------

function f2 = current2 (N,D,P1,P2,L1,L2,R1,R2,V1,V2,start,stop,tol)

order=0;

f2 = quad(@intI2square,start,stop,tol);

    function f2 = intI2square(t);
        f2 = ((V2-exp(-R2/L2*t)*(-R1*N*V2-R1*V2+R2*V1-R2*exp(-R1/L1*P1)*V1+exp(-R1/↩
            L1*P1)*R1*N*V2+exp(-R1/L1*P1)*R1*V2)/R1/(-N-1+exp(-R1/L1*P1)*N*exp(-R2/↩
            L2*P2)+exp(-R1/L1*P1)*exp(-R2/L2*P2)))/R2).^2;
    end
end
```

```
% ------------------------------------
% CALCULATES INTEGRAL OF CURRENT 2
% ------------------------------------

function f3 = current2 (N,D,P1,P2,L1,L2,R1,R2,V1,V2,start,stop,tol)

order=0;

f3 = quad(@intI2,start,stop,tol);

    function f3 = intI2(t);
        f3 = (V2-exp(-R2/L2*t)*(-R1*N*V2-R1*V2+R2*V1-R2*exp(-R1/L1*P1)*V1+exp(-R1/↩
            L1*P1)*R1*N*V2+exp(-R1/L1*P1)*R1*V2)/R1/(-N-1+exp(-R1/L1*P1)*N*exp(-R2/↩
            L2*P2)+exp(-R1/L1*P1)*exp(-R2/L2*P2)))/R2;
    end
end



% ------------------------------------
% CALCULATES INTEGRAL OF CURRENT 1
% ------------------------------------

function f4 = current2 (N,D,P1,P2,L1,L2,R1,R2,V1,V2,start,stop,tol)

order=0;

f4 = quad(@intI1,start,stop,tol);

    function f4 = intI1(t);
        f4 = (V1+exp(-R1/L1*t)*(-R1*N*V2+R1*N*exp(-R2/L2*P2)*V2-R1*V2+R1*exp(-R2/L2↩
            *P2)*V2-exp(-R2/L2*P2)*R2*V1+R2*V1)/(-1+exp(-R1/L1*P1)*exp(-R2/L2*P2))/↩
            R2)/R1;
    end
end
```

A.3 Inductor Optimization

The inductor optimization code was first developed by Ye-Hui Han and then further expanded by David Giuliano. This is a powerful inductor design tool which gives the optimal design for given technical specifications such as inductance, maximum AC and DC currents, and physical dimensions. Due to the length of the code and

the copyright, only the top layer code is provided here. For more information, please contact members of the Perreault group.

```
function [params, dimensions, ploss, warnings] = Inductor_optimize13_wlimit5(op,hc,↩
    di_target,dout,material,temp,type,config)

display('Optimization Starting');

%Constants
u0=4*pi*1e-7;

tspec=temp+273;
rhocu=rhoct(tspec);

%Variables
Bpercent=0.8;
Nmax=config.Nmax;

ur=material.ur;
Bsat=material.Bsat;

idc=op.idc;
ipkpk=op.ipkpk;
ipk=ipkpk/2;
fsw=op.fsw;
L=op.L;

diff_old=10000000;

switch type
    case{'round'}

        filename='MW1000-2000.txt';

        fid=fopen(filename);
        mw_header=textscan(fid,'%s%s%s%s%s%s%s%s%s%s%s%s',1,'Delimiter','\t','↩
            CommentStyle','//');
        mw_values=cell2mat(textscan(fid,'%f%f%f%f%f%f%f%f%f%f%f%f','Delimiter','\t'↩
            ,'CommentStyle','//'));
        fclose(fid);

        insulation = 'single';
        wire_corner = 'nom';
```

```
        AWG = mw_values(:,1);

        switch wire_corner
            case{'min'}
                DCU = mw_values(:,2)*1e-3;
            case{'nom'}
                DCU = mw_values(:,3)*1e-3;
            case{'max'}
                DCU = mw_values(:,4)*1e-3;
        end

        switch insulation
            case{'single'}
                TI = mw_values(:,5)*0.5e-3;
            case{'heavy'}
                TI = mw_values(:,7)*0.5e-3;
            case{'triple'}
                TI = mw_values(:,9)*0.5e-3;
            case{'quad'}
                TI = mw_values(:,11)*0.5e-3;
        end

        dcuMax=DCU(length(DCU));

        Fac=2;
        Fcore=1;

        w_c=0;
        mlast=config.mlast;

    case{'foil','foil2'}
        dcuMin=config.dcuMin;
        dcuMax=config.dcuMax;
        dcuStep=config.dcuStep;

        DCU=dcuMin:dcuStep:dcuMax;
        TI=DCU*0;

        Fac=1;
        Fcore=1;

        w_c=10e-6;
        mlast=config.mlast;
end
```

```
PLOSS = [];
PTOTAL = [];
DIMENSIONS = [];
PARAMS = [];
DIFF = [];
syms di;

for m=1:1:mlast;
    for j=1:1:length(DCU);

        dcu=DCU(j);
        ti=TI(j);

        for N=1:1:Nmax;

            dw=2*ti+dcu;
            h=hc+2*dw;
            d=dout+2*dw;

            if(hc<0)
                continue;
            end

            if(dout<0)
                continue;
            end

            %di=sym2poly(solve(subs('N^2*hc*u0*ur/(2*pi)*log(dout/di)+(di+dout)/4*↩
                u0*(log(8*(dout+di)/(dout-di))-2)=L'),di));
            di=dout/exp(2*pi*L/(N^2*hc*u0*ur));

            diff = abs(di-di_target);
            if diff > diff_old
                continue
            end
            diff_old = diff;

            %check inner diameter
            switch type
                case{'foil'}
                    if(di<2*dcu)
                        continue;
                    end
```

```
    case{'round'}
        if(di<(dmin(N*m)*dw+dw/4))
            continue;
        end
end

%check max B field
Bmax=u0*ur*N*(ipk+idc)/(pi*di);

if(Bmax>Bsat*Bpercent)
    continue;
end

%calculate wire loss
dimensions.type=type;
dimensions.N=N;
dimensions.m=m;
dimensions.di=di;
dimensions.dout=dout;
dimensions.h=h;
dimensions.dcu=dcu;
dimensions.ti=ti;
dimensions.w_c=w_c;

if(strcmp(type,'round'))
    dimensions.awg=AWG(j);
end

[ploss] = Calc_Ind_loss3(dimensions,op,material,rhocu,config);

if isnan(ploss.Ptotal) == 1
    continue
end

%calcuate core temperature rise
Acore=pi/2*(dout^2-di^2)+h*pi*(dout+di);
params.Trise_core=((ploss.Pcore*1000)/(Acore*100*100))^0.833;

%calculate core volume
rcore=(di+dout)/4;
Lcore=pi*2*rcore;
Acore=(dout-di)/2*hc;
params.Vcore=Acore*Lcore;

%calcuate core weight
```

```
cu_density=8.92e6; %g/m^3

switch type

    case{'foil'}
        Vcu_top=dcu*pi/2*(dout^2-di^2);
        Vcu_sides=h*pi/4*((di^2-(di-2*dcu)^2)+((dout+2*dcu)^2-dout^2));
        Vcu_slits=N*w_c*dcu*(2*h+(dout-di));
        params.Vcu=Vcu_top+Vcu_sides-Vcu_slits;
        params.Weight=params.Vcore*material.density+(params.Vcu)*↩
            cu_density;

    case{'foil2'}
        Vcu_top=dcu*pi/2*(dout^2-di^2);
        Vcu_sides=h*pi/4*(di^2+((dout+2*dcu)^2-dout^2));
        Vcu_slits=N*w_c*dcu*(2*h+(dout-di));
        params.Vcu=Vcu_top+Vcu_sides-Vcu_slits;
        params.Weight=params.Vcore*material.density+(params.Vcu)*↩
            cu_density;

    case{'round'}

        Lw=N*(2*hc+dout-di+4*dw);
        Aw=pi*dcu^2/4;
        params.Vcu=m*Lw*Aw;
        params.Weight=params.Vcore*material.density+(params.Vcu)*↩
            cu_density;
        if params.Weight > 0.12
            continue
        end
end

%calculate core flux densities
params.Bavg=u0*ur*N*ipk/(2*pi*rcore);
params.Bmax=Bmax;

%calculate quality factors
Rcore=ploss.Pcore/ipk^2;
Rac=ploss.Pac/ipk^2;
Rdc=ploss.Pdc/idc^2;

params.Qac=2*pi*fsw*L/(Rac+Rcore);
Reff=(ipk^2*(Rac+Rcore)+2*idc^2*Rdc)/(ipk^2+2*idc^2);
params.Qeff=2*pi*fsw*L/Reff;
```

```
            clear di;
            syms di;

            PLOSS=[PLOSS,ploss];
            PTOTAL=[PTOTAL,ploss.Ptotal];
            DIMENSIONS=[DIMENSIONS,dimensions];
            PARAMS=[PARAMS,params];
            DIFF=[DIFF,diff];
        end
    end
end

%[ptotal, int]=min(PTOTAL);
%ploss=PLOSS(int);
%dimensions=DIMENSIONS(int);
%params=PARAMS(int);

[diff, int]=min(DIFF);
ploss=PLOSS(int);
dimensions=DIMENSIONS(int);
params=PARAMS(int);


warnings={};

if(size(ploss)==0)

    %There are NO valid solutions
    warnings{length(warnings)+1}='Warning: No valid solutions!';
    ploss=NaN;
    dimensions=NaN;

else

    %There are valid solutions
    if(dimensions.N==Nmax)
        warnings{length(warnings)+1}='Warning: N max may be too small!';
    end

    if(dimensions.dcu==dcuMax)
        warnings{length(warnings)+1}='Warning: dcu max may be too small!';
    end

    numSol = length(PLOSS);
```

```
    display(strcat(num2str(numSol), ' valid solutions!'));
    display('Optimization Complete');

end
```

Bibliography

[1] S. Roundy, P.K. Wright, and J. Rabaey. A study of low level vibrations as a power source for wireless sensor nodes. *Computer Communications*, 26:1131–1144, 2003.

[2] P.D. Mitcheson, E.K. Reilly, T. Toh, P.K. Wright, and E.M. Yeatman. Performance limits of the three mems inertial energy generator transduction types. *Journal of Micromechanics and Microengineering*, 17:S211–S216, 2007.

[3] J. Kymissis, C. Kendall, J. Paradiso, and N. Gershenfeld. Parasitic power harvesting in shoes. *Second International Symposium on Wearable Computers*, pages 132–139, October 1998.

[4] N.E. DuToit, B.L. Wardle, and S.-G Kim. Design considerations for mems-scale piezoelectric viaration energy harvesters. *Integrated Ferroelectrics*, 2005.

[5] Y.B. Jeon, R. Sood, J.H. Jeong, and S.G. Kim. Mems power generator with transverse mode thin film pzt. *Sensors and Actuators a-Physical*, 122:16–22, 2005.

[6] H. Kloub, D. Hoffmann, B. Folkmer, and Y. Manoli. A micro capacitive vibration energy harvester for low power electronics. *PowerMEMS 2009*, pages 165–168, December 2009.

[7] T. Sterken, K. Baert, R. Puers, G. Borghs, and R. Mertens. A new power mems component with variable capacitance. *Pan Pacific Microelectronics Symposium*, pages 27–34, Feb 2003.

[8] P. Glynne-Jones, M. Tudor, S. Beeby, and N. White. An electromagnetic, vibration-powered generator for intelligent sensor systems. *Sensors and Actuators A*, 110:344–349, Feb 2004.

[9] R. Amirtharajah and A.P. Chandrakasan. Self-powered signal processing using vibration-based power generation. *IEEE Journal of Solid-State Circuits*, 33:687–695, 1998.

[10] T. Reissman and E. Garcia. An ultra-lightweight multi-source power harvesting system for insect cyborg sentinels. *ASME Conference on Smart Materials, Adaptive Structures and Intelligent Systems*, pages 711–718, October 2008.

[11] T. Reissman and E. Garcia. Surgically implanted energy harvesting devices for renewable power sources in insect cyborgs. *ASME International Mechanical Engineering Congress and Exposition.*

[12] N. Ghafouri, H. Kim, M.Z. Atashbar, and K. Najafi. A micro thermoelectric energy scavenger for a hybrid insect. In *Sensors, 2008 IEEE*, pages 1249–1252, Oct. 2008.

[13] J. Montanaro, R.T. Witek, K. Anne, A.J. Black, E.M. Cooper, D.W. Dobberpuhl, P.M. Donahue, J. Eno, G.W. Hoeppner, D. Kruckemyer, T.H. Lee, P. Lin, L. Madden, D. Murray, M.H. Pearce, S. Santhanam, K.J. Snyder, R. Stephany, and S.C. Thierauf. A 160-mhz, 32-b, 0.5-w cmos risc microprocessor. *IEEE Journal of Solid-State Circuits*, 31:1703–1714, 1996.